黒潮続流と伊豆海嶺における密度面を横切る混合と等密度面撹拌効果に関する研究

Master's Thesis

DIAPYCNAL MIXING AND ISOPYCNAL STIRRING IN THE KUROSHIO EXTENSION FRONT AND Izu Ridge

March 2024

Graduate School of Marine Science and Technology
Tokyo University of Marine Science and Technology
Master's Course of Marine Resources and Environment

IKEDA YUKI

Master's Thesis

DIAPYCNAL MIXING AND ISOPYCNAL STIRRING IN THE KUROSHIO EXTENSION FRONT AND IZU RIDGE

March 2024

Graduate School of Marine Science and Technology
Tokyo University of Marine Science and Technology
Master's Course of Marine Resources and Environment

IKEDA YUKI

Contents

1 Introduction

Understanding how water masses, heat, salt, organic and inorganic constituents including nutrients, are stirred, mixed and modified is critical for better predicting how the ocean responds to ongoing climate changes. This is why enormous efforts both in observations and numerical modelings have been devoted to quantify or parameterize the mixing rates in the ocean. The one of the observational advances in such challenges made in 1970's was the development of the methods to quantify vertical eddy diffusivities of the ocean. In these methods, the equations for the turbulent kinetic energy and for the microscale thermal variance were simplified (Osborn 1980[1]; Osborn and Cox 1972[2]). Assuming steady state of thermal variance and the balance among variance production and dissipation, ignoring small transport terms and keeping only production through mean vertical temperature gradient by scaling the production terms, the equation for the thermal variance can be simplified as i.e.,

$$\begin{aligned} 2\overline{w'T'}\frac{\partial \overline{T}}{\partial z} &= k_T \overline{\left(\frac{\partial T'}{\partial x_i}\right)\left(\frac{\partial T'}{\partial x_i}\right)} \\ &= \chi, \end{aligned} \tag{1}$$

where T is temperature with the prime for fluctuations and over bar for mean values, χ microscale thermal variance dissipation rate.

However, several studies pointed out that the balance in (1) may not be accurate in frontal regions, where thermohaline interleaving structures are formed (Gregg 1987[3]; Ruddick et al. 2010 [4]; Joyce 1977 [5]). They pointed out that lateral intrusion caused by various mechanisms, such as mesosocale stirring, internal waves, and double diffusive intrusions, can contribute to the production of thermal variance.

Nagai et al.(2015)[6] conducted intensive field observations using autonomous microstructure profiling floats in the Kuroshio Extension. The results showed that abundant thermohaline interleaving structures are formed presumably caused by meso- and submesoscale stirred along isopycnal surfaces, leading to the vertical thermohaline stratification favorable to the onset of active double-diffusive convection, which acts on a sharp temperature gradient formed by the lateral stirring or intrusive processes and dissipate the thermal variance. Observed microscale temperature variance dissipation rates χ are found to be very large, suggesting that the double-diffusion effectively dissipates the thermal variance fueled by the lateral stirring. However, the above scenario is rather speculative, and needs some quantification on how much isopycnal stirring actually occurs in the Kuroshio Current and how much of the microscale temperature variance generated by meso- and submesoscale stirring and how much is generated through microscale mixing processes such as

turbulence and double-diffusive convection acting on mean and mesoscale temperature fields. To address this issue, the triple decomposition method of Garrett(2001)[7] is employed and applied to the observation data acquired at the Izu Ridge and the Kuroshio Extension, and the isopycnal stirring coefficient for these areas is calculated and compared. This method has been used in many regions where the major ocean currents flow, such as the Southern Ocean (Naveira Garabato et al.,2011[8],2016[9]), as well as Brazil Current (Dorleta Garcia et al.,2023[10]). However, the effect of double diffusive convection, that was reported to be important for tracer mixing in subsurface of the Kuroshio Extension, has yet to be examined in the triple decomposition framework. Thus, the double-diffusive convection is integrated in the triple decomposition method, in this study. The objectives of this research are (1) to clarify the generation and dissipation processes of temperature variance, considering the microscale temperature variance generation rate due to double-diffusive flux and (2) to quantify the intensity of isopycnal stirring in both the Izu Ridge and Kuroshio Extension regions.

2 Methods

2.1 Study area

In this study, two intensive observation dataset obtained using profiling floats along the Kuroshio and the Kuroshio Extension were used. One is in the Kuroshio flowing over the Izu Ridge where the strong turbulence is generated near the ridge that continues in the downstream, and the other is in the Kuroshio Extension, where the northward flowing warm-salty Kuroshio meats cold-fresh Oyashio waters. In Izu Ridge, a Navis Autonomous Profiling Float (Sea-Bird Scientific, Bellevue, WA, USA), equipped with a MicroRider (hereinafter, Navis-MR, Rockland Scientific International, Victoria, BC, Canada), was deployed at $34°N$,$139.7°E$ on June 21, 2017, using R/V Shinsei-Maru (JAMSTEC). It was subsequently advected along the Kuroshio Current flowing over the Izu Ridge, and recovered on June 27, 2017 (Figure 1). Two shear probes and high-resolution thermistors (FPO7) were installed on the MicroRider to measure the microscale vertical velocity shear and temperature vertical gradient, which were used to calculate turbulent kinetic energy dissipation rates ϵ and microscale temperature variance dissipation rates χ. In addtion to the microstructure data, NAVIS float measured conductivity, temperature and depth (CTD). However, due to the setting error of the float, the shear probe data was contaminated by the mechanical noises generated by buoyancy pump. Accordingly, turbulent kinetic energy dissipation rate ϵ was determined by fitting Kraichnan Spectra (Kraichnan, 1968[11]) with the temperature gradient spectra measured by FPO7, using Maximum-Likelihood Method developed by Ruddick (2000)[12].

The observations in the Kuroshio Extension was conducted in July 2013. In addition to Navis-

MR float ,Electro Magnetic Autonomous Profiling Explorers (hereafter EM-APEX) floats were also deployed at ($37.39°N$,$142.90°E$) (Figure2) to measure absolute lateral velocity and CTD data. We used only CTD data from the EM-APEX float in this study. The Navis-MR float obtained 14 profiles over the section from ($37.39°N$,$142.90°E$) to ($36.78°N$,$145.37°E$) for 3 days , while one of the EM-APEX floats obtained 174 profiles over the section from ($37.32°N$,$142.74°E$) to ($36.70°N$,$151.67°E$) for 10 days. Unlike the microscale vertical velocity shear observation in the Izu Ridge, the shear probe worked properly and thus the turbulent kinetic energy dissipation rate ϵ was calculated from integrating the shear spectra along the wavenumber choosing the wavenumber range that does not deviate largely from the Nasmyth model spectrum (Oakey 1982[13]).

2.2 Observational instruments

2.2.1 Navis Autonomous profiling float

The Navis float (Seabird Scientific) is equipped with an SBE 41CP CTD, which continuously measures temperature, conductivity, and pressure as it ascends through the water column.Data is collected at a frequency of 1 Hz, allowing for the generation of vertical profiles of oceanographic variables.To facilitate data transmission and remote monitoring, the Navis Float is equipped with communication systems such as an Iridium Transceiver and GPS. These systems enable real-time data transmission and remote data collection from distant locations, enhancing the accessibility and usability of the collected data. Upon deployment, the Navis Float activates automatically and begins collecting data as it descends into the ocean. This autonomous activation ensures seamless operation and data collection without the need for manual intervention. Although observations were conducted using the Navis float in both the Izu Ridge and Kuroshio Extension regions, we utilized temperature, salinity, and pressure data from the EM-APEX float for the Kuroshio Extension front. This decision was based on the higher horizontal resolution of the EM-APEX float compared to that of the Navis float.

2.2.2 MicroRider

The MicroRider is an instrument package for turbulence measurements and is designed to be mounted on a variety of instrument platforms such as AUV, ROV,CTD. It was installed on the Navis float for our observation.

we only can obtain high resolution vertical velocity shear $\overline{\frac{\partial u_t}{\partial z}}$, $\overline{\frac{\partial v_t}{\partial z}}$ (the overbar denotes the spatiol average over the scale larger than turbulence) from the two shear probes with a sampling frequency of 512Hz, and these two values are used to represent the other distortion terms ($\overline{\left(\frac{\partial u_t}{\partial x}\right)^2}$, $\overline{\left(\frac{\partial v_t}{\partial y}\right)^2}$, $\overline{\left(\frac{\partial w_t}{\partial z}\right)^2}$, $\overline{\left(\frac{\partial u_t}{\partial y}\right)^2}$, $\overline{\left(\frac{\partial v_t}{\partial x}\right)^2}$, $\overline{\left(\frac{\partial w_t}{\partial x}\right)^2}$, $\overline{\left(\frac{\partial w_t}{\partial y}\right)^2}$) assuming isotropic,(Normal strain rate)=$\frac{1}{2}$(Shear strain rate) to get the turbulent kinetic energy dissipation rate ϵ . Similarly, two microscale ther-

mistor sensors (FPO7) with a sampling frequency of 512Hz are also mounted on the MicroRider. Since we only can measure the vertical temperature gradient , we need to assume turbulence as the isotropic as we calculate the microscale temperature variance dissipation rate χ :that is , $\overline{\frac{\partial T_t}{\partial x}} = \overline{\frac{\partial T_t}{\partial y}} = \overline{\frac{\partial T_t}{\partial z}}$.

2.2.3 Electro Magnetic Autonomous Profiling Explorer (EM-APEX) float

The EM-APEX float is a device designed for accurate data collection in oceanographic observations. It combines the APEX profiling float from Teledyne Webb Research Corp. with an electric field sensing system developed by the Applied Physics Laboratory at the University of Washington (APL-UW). The APEX float is utilized for measuring fundamental parameters of the ocean such as temperature, salinity, and pressure.Additionally, the APEX float is capable of profiling the ocean to a maximum depth of 2000 meters, adjusting its buoyancy to ascend and descend according to water depth. The EM-APEX float features electrodes to measure electric fields induced by ocean currents in the Earth's magnetic field. This system allows for precise measurement of ocean current speed and direction. Furthermore, the float is equipped with a Sea-Bird Electronics SBE41CP CTD for temperature and salinity measurements. When on the sea surface, its position is determined via GPS, and the collected data are transmitted through the Iridium global satellite communication system.

2.3 Triple decomposition framework

Variables are decomposed into three components:mean, mesoscale fluctuations, and microscale turbulence (Joyce 1977 [5]; Garrett2001[7]). In the microscale turbulence, scales between few millimeters associated with direct molecular dissipation and a few meters associated with statically unstable overrturns are assigned. Theoretically, this category encompasses fluctuation arising from shear instability, convection, and double-diffusive convection. The mesoscale fluctuation includes mesoscale eddies, internal waves, and vortex modes, with a scale range O(10-100 km). On the other hand, the large scale mean component represents properties of large water masses and the large-scale circulation of the ocean, with a scale range O(100-500 km). To proceed with the triple decomposition derivations, it is necessary to assume the presence of spectral gaps between mean and mesoscale fluctuation, as well as between mesoscale fluctuation and microscale turbulence (Joyce 1977[5]; Davis 1994[14]). Accordingly, tracer C and momentum $\mathbf{u}$ are written as $C = C_m + C_e + C_t$ and $\mathbf{u}_m + \mathbf{u}_e + \mathbf{u}_t$, where subscripts m, e, and t represent the mean, mesoscale fluctuation, and turbulence, respectively. Furthermore, the average over time or spatial scales larger than the turbulent scale but smaller than the mesoscale fluctuation scale is denoted by a tilde($\tilde{}$), and the average over time or spatial scales larger than the mesoscale fluctuation scale but smaller than the

mean scale is denoted by angle brackets ($\langle\rangle$). Substituting these decomposed variables into the tracer budget in a mean field, and averaging over the both spatiotemporal scales yields

$$\frac{\partial C_m}{\partial t} + u_m \cdot \nabla C_m + \nabla \cdot \langle \widetilde{(\mathbf{u}_e + \mathbf{u}_t)(C_e + C_t)} \rangle = k_c \nabla^2 C_m \tag{2}$$

Noting the spectral gaps (e.g.,$\widetilde{C_e C_t} = C_e \widetilde{C_t} = 0$, $\langle C_m C_e \rangle = C_m \langle C_e \rangle = 0$), it can be organized as follows

$$\frac{\partial C_m}{\partial t} + u_m \cdot \nabla C_m - k_c \nabla^2 C_m = -\nabla \cdot \langle \mathbf{u}_e C_e \rangle - \nabla \cdot \langle \mathbf{u}_t C_t \rangle. \tag{3}$$

In the case of a simple advection-diffusion equation, where the RHS of (3) is 0, the rate of change in tracer C, transport by advection, and transport by diffusion are conserved. On the other hand, in the context of tracer budget in the mean field with scale separation, additional contributions arise from tracer fluxes driven by mesoscale fluctuations and turbulence which are denoted as $-\nabla \cdot \langle \mathbf{u}_e C_e \rangle$ and $-\nabla \cdot \langle \mathbf{u}_t C_t \rangle$.

Similarly, by substituting these variables into the tracer budget in a mesoscale and microscale field, multiplying by mesoscale fluctuations, and averaging over both spatiotemporal scales, we obtain,

$$\underbrace{\left\langle C_e \widetilde{\frac{\partial (C_t + C_e)}{\partial t}} \right\rangle}_{①} + \underbrace{\left\langle C_e \widetilde{\frac{\partial u_{mi}(C_e + C_t)}{\partial x_i}} \right\rangle}_{②} + \underbrace{\left\langle C_e \widetilde{\frac{\partial (u_{ti} + u_{ei}) C_m}{\partial x_i}} \right\rangle}_{③} + \underbrace{\left\langle C_e \widetilde{\frac{\partial (u_{ti} + u_{ei})(C_t + C_e)}{\partial x_i}} \right\rangle}_{④}$$
$$\underbrace{- \left\langle C_e \widetilde{\frac{\partial \langle (u_{ti} + u_{ei})(C_t + C_e) \rangle}{\partial x_i}} \right\rangle}_{⑤} = \underbrace{\left\langle C_e k_c \widetilde{\frac{\partial^2 (C_e + C_t)}{\partial x_i^2}} \right\rangle}_{⑥}, \tag{4}$$

where subscripts (i, j) denote the three Cartesian directions. Expanding this equation for each term and applying the spectral gap (e.g.,$\widetilde{C_e C_t} = C_e \widetilde{C_t} = 0$, $\langle C_m C_e \rangle = C_m \langle C_e \rangle = 0$), we obtain the following expression.

$$
\begin{aligned}
① &\rightarrow \frac{1}{2}\frac{\partial\langle C_e^2\rangle}{\partial t} \\
② &\rightarrow \langle C_e\frac{\partial u_{mi}C_e}{\partial x_i}\rangle + \underbrace{\langle C_e\frac{\partial u_{mi}\widetilde{C_t}}{\partial x_i}\rangle}_{0} \\
&\rightarrow \frac{1}{2}\frac{\partial u_{mi}\langle C_e^2\rangle}{\partial x_i} + \frac{1}{2}\langle C_e^2\rangle\underbrace{\frac{\partial u_{mi}}{\partial x_i}}_{0} \rightarrow \frac{1}{2}u_{mi}\frac{\partial\langle C_e^2\rangle}{\partial x_i} \\
\\
③ &\rightarrow \widetilde{\langle C_e\frac{\partial u_{ti}C_m}{\partial x_i}\rangle} + \langle C_e\frac{\partial u_{ei}C_m}{\partial x_i}\rangle \\
&\rightarrow \langle C_e\underbrace{\widetilde{u_{ti}}}_{0}\rangle\frac{\partial C_m}{\partial x_i} + C_m\langle C_e\underbrace{\frac{\partial\widetilde{u_{ti}}}{x_i}}_{0}\rangle + \langle C_e u_{ti}\rangle\frac{\partial C_m}{\partial x_i} + C_m\langle C_e\underbrace{\frac{\partial u_{ei}}{\partial x_i}}_{0}\rangle \\
&\rightarrow \langle C_e u_{ei}\rangle\frac{\partial C_m}{\partial x_i} \\
④ &\rightarrow \widetilde{\langle C_e\frac{\partial u_{ti}C_t}{\partial x_i}\rangle} + \widetilde{\langle C_e\frac{\partial u_{ti}C_e}{\partial x_i}\rangle} + \widetilde{\langle C_e\frac{\partial u_{ei}C_t}{\partial x_i}\rangle} + \widetilde{\langle C_e\frac{\partial u_{ei}C_e}{\partial x_i}\rangle} \\
&\rightarrow \widetilde{\langle C_e u_{ti}\frac{\partial C_t}{\partial x_i}\rangle} + \widetilde{\langle C_e C_t\frac{\partial u_{ti}}{\partial x_i}\rangle} + \langle C_e^2\underbrace{\frac{\partial\widetilde{u_{ti}}}{\partial x_i}}_{0}\rangle + \langle C_e\underbrace{\widetilde{C_t}}_{0}\frac{\partial C_e}{\partial x_i}\rangle \\
&+\langle C_e u_{ei}\underbrace{\frac{\partial\widetilde{C_t}}{\partial x_i}}_{0}\rangle + \langle C_e\underbrace{\widetilde{C_t}}_{0}\frac{\partial u_{ei}}{\partial x_i}\rangle + \langle u_{ei}C_e\frac{\partial C_e}{\partial x_i}\rangle + \langle C_e^2\frac{\partial u_{ei}}{\partial x_i}\rangle \\
&\rightarrow \frac{\partial}{\partial x_i}\langle C_e\widetilde{u_{ti}C_t}\rangle - \widetilde{\langle u_{ti}C_t}\frac{\partial C_e}{\partial x_i}\rangle + \frac{1}{2}\frac{\partial}{\partial x_i}\langle u_{ei}C_e^2\rangle \\
⑤ &\rightarrow -\underbrace{\langle C_e\rangle}_{0}\frac{\partial\widetilde{\langle u_{ti}C_t\rangle}}{\partial x_i} - \underbrace{\langle C_e\rangle}_{0}\frac{\partial\widetilde{\langle u_{ti}C_e\rangle}}{\partial x_i} - \underbrace{\langle C_e\rangle}_{0}\frac{\partial\widetilde{\langle u_{ei}C_t\rangle}}{\partial x_i} - \underbrace{\langle C_e\rangle}_{0}\frac{\partial\widetilde{\langle u_{ei}C_e\rangle}}{\partial x_i} \\
&\rightarrow 0 \\
⑥ &\rightarrow \langle C_e k_c\frac{\partial^2 C_e}{\partial x_i^2}\rangle + \langle C_e k_c\underbrace{\frac{\partial^2\widetilde{C_t}}{\partial x_i^2}}_{0}\rangle \rightarrow \frac{\partial}{\partial x_i}\langle k_c C_e\frac{\partial C_e}{\partial x_i}\rangle - k_c\langle\left|\frac{\partial C_e}{\partial x_i}\right|^2\rangle.
\end{aligned}
\tag{5}
$$

By organizing ①-⑥, we obtain mesoscale tracer variance budget.

$$
\begin{aligned}
&\frac{1}{2}\left(\frac{\partial}{\partial t} + u_{mi}\frac{\partial}{\partial x_i}\right)\langle C_e^2\rangle + \frac{\partial}{\partial x_i}\left(\frac{1}{2}\langle u_{ei}C_e^2\rangle + \langle C_e\widetilde{u_{ti}C_t}\rangle - k_c\langle C_e\frac{\partial C_e}{\partial x_i}\rangle\right) \\
&\qquad = -\langle C_e u_{ei}\rangle\frac{\partial C_m}{\partial x_i} + \widetilde{\langle u_{ti}C_t}\frac{\partial C_e}{\partial x_i}\rangle - k_c\langle\left|\frac{\partial C_e}{\partial x_i}\right|^2\rangle.
\end{aligned}
\tag{6}
$$

The first term on the RHS of (6) represents the tracer variance generation by mesoscale tracer flux acting on the mean tracer gradient, whereas the second term of RHS is the tracer variance loss by microscale turbulence acting on the mesoscale tracer gradient. On the other hand, the microscale tracer variance can be obtained by multiplying microscale tracer by the tracer budget in a microscale and mesoscale field, and averaging over both spatiotemporal scales.

$$\underbrace{\left\langle \widetilde{C_t \frac{\partial(C_t + C_e)}{\partial t}} \right\rangle}_{①} + \underbrace{\left\langle \widetilde{C_e \frac{\partial u_{mi}(C_e + C_t)}{\partial x_i}} \right\rangle}_{②} + \underbrace{\left\langle \widetilde{C_t \frac{\partial (u_{ti} + u_{ei}) C_m}{\partial x_i}} \right\rangle}_{③} + \underbrace{\left\langle \widetilde{C_t \frac{\partial (u_{ti} + u_{ei})(C_t + C_e)}{\partial x_i}} \right\rangle}_{④}$$
$$- \underbrace{\left\langle \frac{C_t \partial \widetilde{\langle (u_{ti} + u_{ei})(C_t + C_e) \rangle}}{\partial x_i} \right\rangle}_{⑤} = \underbrace{\left\langle \widetilde{C_t k_c \frac{\partial^2 (C_e + C_t)}{\partial x_i^2}} \right\rangle}_{⑥} \tag{7}$$

Expanding this equation for each term and applying the spectral gap (e.g.,$\widetilde{C_e C_t} = C_e \widetilde{C_t} = 0$, $\langle C_m C_e \rangle = C_m \langle C_e \rangle = 0$), we obtain the following expression.

$$\begin{aligned}
① &\to \frac{1}{2} \frac{\partial \widetilde{\langle C_t^2 \rangle}}{\partial t} \to \frac{1}{2} \frac{\partial \langle C_t^2 \rangle}{\partial t} \\
② &\to \langle \underbrace{\widetilde{C_t}}_{0} \frac{\partial u_{mi} C_e}{\partial x_i} \rangle + \langle \widetilde{C_t \frac{\partial u_{mi} C_t}{\partial x_i}} \rangle \\
&\to \langle \widetilde{C_t^2} \underbrace{\frac{\partial u_{mi}}{\partial x_i}}_{0} \rangle + \frac{1}{2} u_{mi} \frac{\partial \widetilde{\langle C_{ti}^2 \rangle}}{\partial x_i} \to \frac{1}{2} u_{mi} \frac{\partial \langle C_{ti}^2 \rangle}{\partial x_i} \\
③ &\to \langle \widetilde{C_t \frac{\partial u_{ti} C_m}{\partial x_i}} \rangle + \langle \underbrace{\widetilde{C_t}}_{0} \frac{\partial u_{ei} C_m}{\partial x_i} \rangle \\
&\to \langle \widetilde{C_t u_{ti}} \rangle \frac{\partial C_m}{\partial x_i} + C_m \langle C_t \underbrace{\frac{\partial \widetilde{u_{ti}}}{\partial x_i}}_{0} \rangle \\
&\to \langle C_t u_{ti} \rangle \frac{\partial C_m}{\partial x_i} \\
④ &\to \langle \widetilde{C_t \frac{\partial u_{ti} C_t}{\partial x_i}} \rangle + \langle \widetilde{C_t \frac{\partial u_{ti} C_e}{\partial x_i}} \rangle + \langle \widetilde{C_t \frac{\partial u_{ei} C_t}{\partial x_i}} \rangle + \langle \widetilde{C_t \frac{\partial u_{ei} C_e}{\partial x_i}} \rangle \\
&\to \langle \widetilde{C_t u_{ti} \frac{\partial C_t}{\partial x_i}} \rangle + \langle \widetilde{C_t^2 \underbrace{\frac{\partial u_{ti}}{\partial x_i}}_{0}} \rangle + \langle \widetilde{C_t u_{ti}} \frac{\partial C_e}{\partial x_i} \rangle + \langle \widetilde{C_t C_e \underbrace{\frac{\partial u_{ti}}{\partial x_i}}_{0}} \rangle \\
&\to \langle u_{ei} \widetilde{C_t \frac{\partial C_t}{\partial x_i}} \rangle + \langle \widetilde{C_t^2 \underbrace{\frac{\partial u_{ei}}{\partial x_i}}_{0}} \rangle + \langle \underbrace{\widetilde{C_t}}_{0} u_{ei} \frac{\partial C_e}{\partial x_i} \rangle + \langle \widetilde{C_t} C_e \underbrace{\frac{\partial u_{ei}}{\partial x_i}}_{0} \rangle \\
&\to \frac{1}{2} \frac{\partial}{\partial x_i} \langle C_t^2 u_{ti} \rangle + \langle \widetilde{C_t u_{ti}} \frac{\partial C_e}{\partial x_i} \rangle + \frac{1}{2} \frac{\partial}{\partial x_i} \langle u_{ei} \widetilde{C_t^2} \rangle \\
⑤ &\to - \left\langle \frac{\widetilde{C_t \partial \langle u_{ti} C_t \rangle}}{\partial x_i} \right\rangle - \langle \underbrace{\widetilde{C_t}}_{0} \frac{\partial \langle u_{ei} C_e \rangle}{\partial x_i} \rangle \to - \langle \underbrace{\widetilde{C_t}}_{0} \rangle \frac{\partial \langle u_{ti} C_t \rangle}{\partial x_i} \to 0 \\
⑥ &\to \langle \underbrace{\widetilde{C_t}}_{0} k_c \frac{\partial^2 C_e}{\partial x_i^2} \rangle + \langle \widetilde{C_t k_c \frac{\partial^2 C_t}{\partial x_i^2}} \rangle \to \frac{\partial}{\partial x_i} \left(k_c \langle C_t \frac{\partial C_t}{\partial x_i} \rangle \right) - k_c \langle \left| \frac{\partial C_t}{\partial x_i} \right|^2 \rangle
\end{aligned} \tag{8}$$

By organizing ①-⑥, we obtain microscale tracer variance budget.

$$\begin{aligned}\frac{1}{2}\left(\frac{\partial}{\partial t}+u_{mi}\frac{\partial}{\partial x_i}\right)\langle C_t^2\rangle+\frac{\partial}{\partial x_i}\left(\frac{1}{2}\langle u_{ti}C_t^2\rangle+\frac{1}{2}\langle u_{ei}\widetilde{C_t^2}\rangle-k_c\langle C_t\frac{\partial C_t}{\partial x_i}\rangle\right)\\ =-\langle C_t u_{ti}\rangle\frac{\partial C_m}{\partial x_i}-\langle\widetilde{u_{ti}C_t}\frac{\partial C_e}{\partial x_i}\rangle-k_c\langle\left|\frac{\partial C_t}{\partial x_i}\right|^2\rangle\end{aligned} \tag{9}$$

(6) is referred to as mesoscale tracer variance budget, and (9) is referred to as microscale tracer variance budget. Considering the tracer as potential temperature and assuming steady state as well as spatial uniformity, we neglect the terms related to temporal variations and divergence so that we can evaluate the variance budget. Ultimately, (6) and (9) can be expressed as follows.

$$\langle\mathbf{u_e}\theta_e\rangle\cdot\nabla\theta_m-\langle\widetilde{\mathbf{u_t}\theta_t}\cdot\nabla\theta_e\rangle=0 \tag{10}$$

$$\langle\mathbf{u_t}\theta_t\rangle\cdot\nabla\theta_m+\langle\widetilde{\mathbf{u_t}\theta_t}\cdot\nabla\theta_e\rangle=-\frac{1}{2}\langle\chi\rangle, \tag{11}$$

where microscale temperature variance dissipation rate $\chi = 2k_\theta\left|\nabla\theta_t\right|^2$. (10) expresses that all mesoscale variance transported from the mean is entirely transferred to microscale variance, while (11) expresses that microscale variances generated by turbulence acting on both mean and mesoscale temperature gradient are dissipated at microscale.

To estimate these terms from microstructure data, we need to apply the flux-gradient assumption using diapycnal eddy diffusivity K_ρ and isopycnal stirring coefficient K_e ; that is,

$$-K_e\left|\nabla_{||}\theta_m\right|^2-\langle-K_\rho\left|\nabla_\perp\theta_e\right|^2\rangle=0 \tag{12}$$

$$-K_\rho\left|\nabla_\perp\theta_e\right|^2+\langle-K_\rho\left|\nabla_\perp\theta_e\right|^2\rangle=-\frac{1}{2}\langle\chi\rangle, \tag{13}$$

where the turbulent fluxes of temperature averaged over large scale is represented by the diapycnal gradient of large scale mean temperature $\langle\mathbf{u_t}\theta_t\rangle\sim-K_\rho\nabla_\perp\theta_m$ and the mesoscale fluxes of temperature averaged over large scale mean temperature is represented by the isopycnal gradient of the mesoscale temperature $\langle\mathbf{u_e}\theta_e\rangle\sim-K_e\nabla_{||}\theta_m$.

Generally, the spatial scale of mesoscale eddy is O(10 km)-O(100 km) which is much larger than the vertical scale of the ocean. Polzin and Ferrari (2004)[15] showed that the flux associated with vortical modes and internal waves is several orders of magnitude less than that of balanced mesoscale eddies. Considering these facts, lateral velocity dominates the mesoscale velocity. Even if mesoscale vertical flow acts on the vertical mean temperature gradient through $-\langle w_e\theta_e\rangle\,\partial C_m/\partial z$ in (10), mesoscale temperature variance can not be generated as $w_e \ll u_e$. In this regard, the gradient of the variance generation term from mean to mesoscale can be considered along isopycnals, $K_e\left|\nabla_{||}\theta_m\right|^2$.

The schematic diagram of temperature variance transport is depicted in the Figure 4. Turbulent fluxes act on the mean-scale temperature gradient and directly generate microscale temperature variance $K_\rho \left|\nabla_\perp \theta_m\right|^2$. On the other hand, mesoscale temperature fluxes similarly act on the mean-scale temperature gradient, generating mesoscale temperature variance$K_e \left|\nabla_{||} \theta_m\right|^2$. Subsequently, turbulent fluxes acting on the mesoscale temperature gradient lead to the generation of microscale temperature variance$\langle -K_\rho \left|\nabla_\perp \theta_e\right|^2 \rangle$. The generated temperature variances eventually dissipate through molecular processes$-\frac{1}{2}\langle \chi \rangle$.

In this paper, we further attempted to dissect production of temperature variance caused by microscale fluctuations into contributions from double-diffusive convection and from mechanical turbulence, and aimed to quantify the contribution of double-diffusion to the generation of temperature variance.

Denoting the potential temperature and velocity of the double diffusion as θ_{dd} and $\mathbf{u}_{dd}$, respectively, mesoscale temperature variance budget (10) can be rewritten as follows,

$$\langle \mathbf{u_e} \theta_e \cdot \nabla \theta_m \rangle - \langle \widetilde{\mathbf{u_t} \theta_t} \cdot \nabla \theta_e \rangle - \langle \widetilde{\mathbf{u_{dd}} \theta_{dd}} \cdot \nabla \theta_e \rangle - \langle \widetilde{\mathbf{u_t} \theta_{dd}} \cdot \nabla \theta_e \rangle - \langle \widetilde{\mathbf{u_{dd}} \theta_t} \cdot \nabla \theta_e \rangle = 0 \tag{14}$$

Similarly, the microscale temperature variance budget (11) is also rewritten as

$$\begin{aligned} &\langle \mathbf{u_t} \theta_t \rangle \cdot \nabla \theta_m + \langle \mathbf{u_{dd}} \theta_{dd} \rangle \cdot \nabla \theta_m + \langle \mathbf{u_{dd}} \theta_t \rangle \cdot \nabla \theta_m + \langle \mathbf{u_t} \theta_{dd} \rangle \cdot \nabla \theta_m \\ &+ \langle \widetilde{\mathbf{u_t} \theta_t} \cdot \nabla \theta_e \rangle + \langle \widetilde{\mathbf{u_{dd}} \theta_{dd}} \cdot \nabla \theta_e \rangle + \langle \widetilde{\mathbf{u_t} \theta_{dd}} \cdot \nabla \theta_e \rangle + \langle \widetilde{\mathbf{u_{dd}} \theta_t} \cdot \nabla \theta_e \rangle = -\frac{1}{2} \langle \chi \rangle. \end{aligned} \tag{15}$$

For both the equations (14) and (15), additional terms appear that represent the temperature variance generation due to the interaction between double diffusion and turbulence. Quantifying these terms is challenging, and the coexistence of double diffusion and turbulence is not yet fully understood. Therefore, by utilizing the buoyancy Reynolds number Re_b and Turner angle Tu, we separated the regions where potential temperature flux occurs due to double diffusion and turbulence. We assumed that the flux where $Re_b < 200$ and $|\mathrm{Tu}| > 45°$ is attributed to double diffusion, while the flux where $Re_b > 200$ or $|\mathrm{Tu}| < 45°$ is associated with mechanical turbulence. Consequently, the temperature variance generation terms due to the interaction between double diffusion and turbulence is neglected. Expressing the double-diffusion induced temperature flux using the effective temperature diffusivity K_{dd} developed by Radko and smith (2012)[16] and Fedorov (1988)[17], (14) and (15) can be transformed as follows.

$$-K_e \left|\nabla_{||} \theta_m\right|^2 - \langle -K_\rho \left|\nabla_\perp \theta_e\right|^2 \rangle - \langle -K_{dd} \left|\nabla_\perp \theta_e\right|^2 \rangle = 0 \tag{16}$$

$$-K_\rho \left|\nabla_\perp \theta_m\right|^2 - K_{dd} \left|\nabla_\perp \theta_m\right|^2 + \langle -K_\rho \left|\nabla \perp \theta_e\right|^2 \rangle + \langle -K_{dd} \left|\nabla \perp \theta_e\right|^2 \rangle = -\frac{1}{2} \langle \chi \rangle \tag{17}$$

(16) and (17) represent the budget equations for mesoscale and microscale temperature variance taking into account double diffusive convection, respectively, and are referred to throughout this paper. The schematic diagram of temperature variance transport is depicted in the Figure 5. The diapycnal turbulent diffusivity K_ρ is estimated by the model introduced by Osborn(1980) [1] which will be explained in the next section. The isopycnal stirring coefficient K_e is calculated from the microscale temperature variance budget obtained simply by adding (16) to (17).

$$K_e = \frac{\frac{1}{2}\chi - K_\rho \left|\nabla_\perp \theta_m\right|^2 - K_{dd} \left|\nabla_\perp \theta_m\right|^2}{\left|\nabla_{||} \theta_m\right|^2}. \tag{18}$$

The double-diffusion-induced thermal diffusivity K_{dd} is estimated by two parameterizations developed by Radko and Smith(2012)[16] and Fedorov(1988)[17].

2.4 Vertical turbulent diffusivity K_ρ estimated from turbulent kinetic energy (TKE) dissipation rate ϵ

Turbulent kinetic energy (TKE) dissipation rate ϵ was inferred from the vertical microscopic velocity shear measured by two shear probes which were installed on the MicroRider on the NAVIS-MR float during the July 2013 Kuroshio Extension cruise. From the perspective of triple decomposition, the velocities in the observation can be divided into three components: turbulent $\mathbf{u_t}$, mesoscale $\mathbf{u_e}$, and mean $\mathbf{u_m}$. When we calculate high-resolution vertical shear of them, the velocity shear associated with mesoscale and mean components becomes negligibly small compared to the turbulent shear ($\frac{d\mathbf{u_t}}{dz} \gg \frac{d\mathbf{u_e}}{dz}, \frac{d\mathbf{u_m}}{dz}$). Therefore, observed velocity shear is turbulent shear ($\frac{d\mathbf{u}}{dz} \sim \frac{d\mathbf{u_t}}{dz}$), and TKE dissipation rate ϵ is calculated from turbulent shear variance $\overline{\left(\frac{d\mathbf{u_t}}{dz}\right)^2}$ by assuming isotropic.

$$\begin{aligned} \epsilon &= \frac{15}{4}\nu \left[\overline{\left(\frac{du_t}{dz}\right)^2} + \overline{\left(\frac{dv_t}{dz}\right)^2}\right], \\ \overline{\left(\frac{d\mathbf{u_t}}{dz}\right)^2} &= \int_{k_o}^{k_c} \phi_{\frac{d\mathbf{u_t}}{dz}}\, dk, \end{aligned} \tag{19}$$

where overbar denotes spatiotemporal average over the scale larger than turbulence, and $\mathbf{u_t}$ is horizontal turbulent velocity. Turbulent shear variance $\overline{\left(\frac{d\mathbf{u_t}}{dz}\right)^2}$ is calculated integrating the measured turbulent shear spectra $\phi_{\frac{d\mathbf{u_t}}{dz}}$ along the vertical wavenumber k from the lowest wavenumber $k_o = 1[cpm]$ to the highest wavenumber k_c.

While the measurement of microscale velocity shear was unsuccessful during the June 2017 Izy Ridge cruise, successful measurement was achieved for microscale temperature gradient using FPO7.

Consequently,TKE dissipation rate ϵ was estimated by fitting Kraichnan spectrum to the observed spectra following maximum likelihood method[18].

By applying triple decomposition to the turbulent momentum equation,

$$\begin{aligned}
&\underbrace{\langle u_{ti}\widetilde{\frac{\partial\left(u_{ei}+u_{ti}\right)}{\partial t}}\rangle}_{①}+\underbrace{\langle u_{ti}u_{mj}\widetilde{\frac{\partial(u_{ei}+u_{ti})}{\partial x_j}}\rangle}_{②}+\underbrace{\langle u_{ti}\widetilde{\left(u_{tj}+u_{ej}\right)\frac{\partial u_{mi}}{\partial x_j}}\rangle}_{③}\\
&\underbrace{+\langle u_{ti}\widetilde{\left(u_{tj}+u_{ej}\right)\frac{\partial\left(u_{ti}+u_{ei}\right)}{\partial x_j}}\rangle}_{④}\underbrace{-\langle u_{ti}\frac{\partial}{\partial x_j}\langle\widetilde{\left(u_{ti}+u_{ei}\right)\left(u_{tj}+u_{ej}\right)}\rangle\rangle}_{⑤}\\
&=\underbrace{-\langle u_{ti}\widetilde{\frac{1}{\rho_o}\frac{\partial\left(P_t+P_e\right)}{\partial x_i}}\rangle}_{⑥}+\underbrace{\langle\widetilde{u_{ti}\left(b_e+b_t\right)\mathbf{k}}\rangle}_{⑦}+\underbrace{\langle u_{ti}\nu\widetilde{\frac{\partial^2\left(u_{ti}+u_{ei}\right)}{\partial x_j^2}}\rangle}_{⑧},
\end{aligned}\tag{20}$$

where $\mathbf{k}$ is the unit vector in the vertical direction, P is pressure , and b is buoyancy. Expanding this equation for each term and applying the spectral gap (e.g.,$\widetilde{C_eC_t}=C_e\widetilde{C_t}=0$, $\langle C_mC_e\rangle = C_m\langle C_e\rangle=0$), we obtain the following expression.

$$\begin{aligned}
①&\rightarrow\frac{1}{2}\frac{\partial}{\partial t}\langle\widetilde{u_{ti}^2}\rangle\rightarrow\frac{1}{2}\frac{\partial}{\partial t}\langle u_{ti}^2\rangle\\
②&\rightarrow\langle\underbrace{\widetilde{u_{ti}}}_{0}u_{mj}\frac{\partial u_{ei}}{\partial x_j}\rangle+u_{mj}\langle\widetilde{u_{ti}\frac{\partial u_{ti}}{\partial x_j}}\rangle\rightarrow\frac{1}{2}u_{mj}\frac{\partial}{\partial x_j}\langle u_{ti}^2\rangle\\
③&\rightarrow\langle\widetilde{u_{ti}u_{tj}}\rangle\frac{\partial u_{mi}}{\partial x_j}+\langle\underbrace{\widetilde{u_{ti}}}_{0}u_{ej}\rangle\frac{\partial u_{mi}}{\partial x_j}\rightarrow\langle u_{ti}u_{tj}\rangle\frac{\partial u_{mi}}{\partial x_j}\\
④&\rightarrow\langle\widetilde{u_{ti}u_{tj}\frac{\partial u_{ti}}{\partial x_j}}\rangle+\langle\widetilde{u_{ti}u_{tj}}\frac{\partial u_{ei}}{\partial x_j}\rangle+\langle u_{ej}\widetilde{u_{ti}\frac{\partial u_{ti}}{\partial x_j}}\rangle+\langle\underbrace{\widetilde{u_{ti}}}_{0}u_{ej}\frac{\partial u_{ei}}{\partial x_j}\rangle\\
&\rightarrow\frac{1}{2}\frac{\partial}{\partial x_j}\langle\widetilde{u_{ti}^2u_{tj}}\rangle-\frac{1}{2}\langle\widetilde{u_{ti}^2\underbrace{\frac{\partial u_{tj}}{\partial x_j}}_{0}}\rangle+\langle\widetilde{u_{ti}u_{tj}}\frac{\partial u_{ei}}{\partial x_j}\rangle+\frac{1}{2}\frac{\partial}{\partial x_j}\langle\widetilde{u_{ti}^2}u_{ej}\rangle-\frac{1}{2}\langle\widetilde{u_{ti}^2}\underbrace{\frac{\partial u_{ej}}{\partial x_j}}_{0}\rangle\\
&\rightarrow\frac{1}{2}\frac{\partial}{\partial x_j}\langle u_{ti}^2u_{tj}\rangle+\langle\widetilde{u_{ti}u_{tj}}\frac{\partial u_{ei}}{\partial x_j}\rangle+\frac{1}{2}\frac{\partial}{\partial x_j}\langle\widetilde{u_{ti}^2}u_{ej}\rangle\\
⑤&\rightarrow-\langle\underbrace{\widetilde{u_{ti}}}_{0}\frac{\partial}{\partial x_j}\langle\widetilde{u_{ti}u_{tj}}\rangle\rangle-\langle\underbrace{\widetilde{u_{ti}}}_{0}\frac{\partial}{\partial x_j}\langle u_{ei}u_{ej}\rangle\rangle\rightarrow0\\
⑥&\rightarrow-\frac{1}{\rho_0}\langle u_{ti}\frac{\partial P_t}{\partial x_i}\rangle-\frac{1}{\rho_0}\langle\underbrace{\widetilde{u_{ti}}}_{0}\frac{\partial P_e}{\partial x_i}\rangle\rightarrow-\frac{1}{\rho_0}\left(\frac{\partial}{\partial x_i}\langle u_{ti}P_t\rangle-\langle P_t\underbrace{\frac{\partial u_{ti}}{\partial x_i}}_{0}\rangle\right)\\
&\rightarrow-\frac{1}{\rho_0}\frac{\partial}{\partial x_i}\langle u_{ti}P_t\rangle\\
⑦&\rightarrow\langle\underbrace{\widetilde{w_t}}_{0}b_e\rangle+\langle w_tb_t\rangle\rightarrow\langle w_tb_t\rangle\\
⑧&\rightarrow\langle u_{ti}\nu\frac{\partial^2u_{ti}}{\partial x_j^2}\rangle+\langle\underbrace{\widetilde{u_{ti}}}_{0}\nu\frac{\partial^2u_{ei}}{\partial x_j^2}\rangle\rightarrow2\nu\frac{\partial}{\partial x_j}\langle u_{ti}e_{ij}\rangle-2\nu\langle e_{ij}e_{ij}\rangle
\end{aligned}\tag{21}$$

By organizing ①-⑧, we obtain turbulent kinetic energy budget in terms of the triple decomposition.

$$\begin{aligned}\frac{1}{2}\left(\frac{\partial}{\partial t}+u_{mj}\frac{\partial}{\partial x_j}\right)\langle u_{ti}^2\rangle = -\frac{\partial}{\partial x_j}\left(\frac{1}{\rho_o}\langle P_t u_{tj}\rangle+\frac{1}{2}\langle u_{ti}^2 u_{tj}\rangle+\frac{1}{2}\langle\widetilde{u_{ti}^2}u_{ej}\rangle-2\nu\langle u_{ti}e_{ij}\rangle\right)\\ -\langle u_{ti}u_{tj}\rangle\frac{\partial u_{mi}}{\partial x_j}-\langle\widetilde{u_{ti}u_{tj}}\frac{\partial u_{ei}}{\partial x_j}\rangle+\langle w_t b_t\rangle-2\nu\langle e_{ij}e_{ij}\rangle,\end{aligned} \tag{22}$$

where $e_{ij}=\frac{1}{2}\left(\frac{\partial u_{ti}}{\partial x_j}+\frac{\partial u_{tj}}{\partial x_i}\right)$ is the turbulent strain rate and the subscripts(i, j) denote the three Cartesian directions. Here, the last term on the RHS of (22) can also be written as follows.

$$\begin{aligned}-2\nu\langle e_{ij}e_{ij}\rangle &= -2\nu\langle\frac{1}{4}\left(\frac{\partial u_{ti}}{\partial x_j}\right)^2+\frac{1}{2}\frac{\partial u_{ti}}{\partial x_j}\frac{\partial u_{tj}}{\partial x_i}+\frac{1}{4}\left(\frac{\partial u_{tj}}{\partial x_i}\right)^2\rangle\\ &= -2\nu\langle\frac{1}{2}\frac{\partial u_{ti}}{\partial x_j}\left(\frac{\partial u_{ti}}{\partial x_j}+\frac{\partial u_{tj}}{\partial x_i}\right)-\frac{1}{4}\left(\underbrace{\left(\frac{\partial u_{ti}}{\partial x_j}\right)^2-\left(\frac{\partial u_{tj}}{\partial x_i}\right)^2}_{0}\right)\rangle\\ &= -\nu\langle\frac{\partial u_{ti}}{\partial x_j}\left(\frac{\partial u_{ti}}{\partial x_j}+\frac{\partial u_{tj}}{\partial x_i}\right)\rangle\end{aligned} \tag{23}$$

This is so-called TKE dissipation rate ϵ. If we apply isotropic assumption to this form of ϵ, it can be transformed as (19). The second and third terms on the RHS of (22) represent the TKE production rate caused by turbulent Reynolds stress acting on the mean and mesoscale velocity gradients, respectively. When $\frac{\partial u_{mi}}{\partial x_i}$ or $\frac{\partial u_{ei}}{\partial x_i}$ is positive, the turbulence stress $\langle\widetilde{u_{ti}u_{tj}}\rangle$ tend to be negative. This means that these terms tend to be positive, and mean and mesoscale kinetic energy are likely to be extracted and converted into turbulent kinetic energy through these processes. The fourth term on the RHS of (22) is called buoyancy destruction/production term. When this term is negative, i.e., buoyancy distraction, turbulent kinetic energy is consumed to break the stratification bringing buoyant water down and less buoyant water up, lifting up the center of gravity that increase the potential energy. On the other hand, when this term is positive, i.e, buoyancy production, convective mixing occurs for example by surface cooling, sinking dense water down and buoyant water up, converting potential energy to TKE. Under the assumption of steady state and homogeneity, we ignore the time-dependent and divergence terms.

$$\langle\widetilde{u_{ti}u_{tj}}\rangle\frac{\partial u_{mi}}{\partial x_i}+\langle\widetilde{u_{ti}u_{tj}}\frac{\partial u_{ei}}{\partial x_i}\rangle=\langle w_t b_t\rangle-\langle\epsilon\rangle \tag{24}$$

Let us denote the fraction of turbulent energy loss required to elevate mean potential energy, relative to the turbulent energy production arising from mean and mesoscale kinetic energy, as the flux Richardson number R_f, as also known as the mixing efficiency,

$$R_f=\frac{\langle w_t b_t\rangle}{\langle\widetilde{u_{ti}u_{tj}}\rangle\frac{\partial u_{mi}}{\partial x_i}+\langle\widetilde{u_{ti}u_{tj}}\frac{\partial u_{ei}}{\partial x_i}\rangle}, \tag{25}$$

and substitute (25) into (24) resulting in

$$\langle w_t b_t \rangle = -\Gamma_t \langle \epsilon \rangle, \tag{26}$$

where $\Gamma_t = \frac{R_f}{1-R_f}$ is the mixing coefficient or the dissipation ratio (St. Laurent and Schumitt 1999[19]). The mixing coefficient, Γ_t represents the ratio of turbulent buoyancy destruction to the TKE dissipation rate. However, in regions where double-diffusive convection occurs, additional buoyancy fluxes come into play, leading to an increase in Γ_t For instance, $\Gamma_t > 0.2$ under the condition of $1 < R_\rho < 2$ and $Ri > 1$ [19]. In this study, we adopted $\Gamma_t = 0.2$ as the typical value in the real ocean to estimate buoyancy fluxes. Turbulent buoyancy fluxes can also be represented by flux-gradient relationship using diapycnal turbulent diffusivity for density, K_ρ.

$$\langle w_t b_t \rangle = -K_\rho \frac{\partial b_m}{\partial z} \tag{27}$$

By substituting this relationship into (26), we can express diapycnal turbulent diffusivity K_ρ by TKE dissipation rate ϵ and buoyancy vertical gradient, and the mixing coefficient Γ_t.

$$K_\rho = \Gamma_t \frac{\epsilon}{\frac{\partial b_m}{\partial z}} \tag{28}$$

2.5 Microscale temperature variance dissipation rate χ inferred from micro-temperature (FPO7)

The microscale temperature variance dissipation rate χ is calculated from variance of microscale temperature gradient,which is obtained by integrating temperature gradient spectra.

$$\begin{aligned} \chi &= 6 k_T \overline{\left(\frac{dT_t}{dz} \right)^2} \\ \overline{\left(\frac{dT_t}{dz} \right)^2} &= \int_{k_1}^{k_2} \phi_{\frac{dT_t}{dz}} dk, \end{aligned} \tag{29}$$

where k_T is the molecular diffusivity for heat $\left(m^2/s\right)$, $\frac{dT_t}{dz}$ is the microscale temperature vertical gradient, and $\phi_{\frac{dT_t}{dz}}$ is the wavenumber spectrum of the temperature vertical gradient. The observed temperature includes temperature variations at all scales, but as soon as we calculate microscale gradient, we can ignore mesoscale and mean temperature gradient. Since the microscale velocity shear observed in the Izu-Ogasawara Ridge was contaminated by noise, turbulent kinetic energy dissipation rate ϵ was estimated from χ. Specifically, Kraichnan spectrum [11] is fitted to the computed spectra by the maximum likelihood method [18] to obtain the batchelar wave number

k_b. Thus, turbulent kinetic energy dissipation rate can be calculated as $\epsilon = \nu k_T^2 k_b^4$.

2.6 Parameterizations of the double-diffusion-induced thermal diffusivity K_{dd}

Double-diffusive convection depends on how temperture and salinity stack vertically, that is characterized by the density ratio R_ρ,

$$R_\rho = \frac{\alpha \frac{d\theta}{dz}}{\beta \frac{dS}{dz}}, \tag{30}$$

where α is the thermal expansion coefficient and β is the haline contraction coefficient. R_ρ represents the ratio of how much water temperature and salinity contribute to the vertical change in density. In the Figure 6 with $\beta \frac{dS}{dz}$ on the horizontal axis and $\alpha \frac{d\theta}{dz}$ on the vertical axis, salt finger favorable condition is made in the range of $1 < R_\rho < +\infty$, and diffusive convection favorable condition is made in the range of $0 < R_\rho < 1$. When classifying conditions of double diffusion using R_ρ, a challenge arises due to the presence of singularity. This problem can be removed introducing Turner angle Tu [20],[21]. The Turner angle is a simple representation of R_ρ in terms of an angle without a such singularity.

$$Tu = \arctan\left(\alpha\delta\theta - \beta\delta S, \alpha\delta\theta + \beta\delta S\right), \tag{31}$$

where arctan represents four-quadrant arctangent. The infinite R_ρ value is replaced by the finite values, π and $-\pi$. The salt finger favorable condition is in the range of $45° < Tu < 90°$, whereas the diffusive convection favorable condition is in the range of $-90° < Tu < -45°$. In this study, two parameterizations developed by [16] and[17] were used to estimate the thermal diffusivity induced by double diffusive convection K_{dd}. The salt finger-induced thermal diffusivity was parameterized by [16] as follows.

$$\begin{aligned} F_s &= \frac{a_s}{\sqrt{R_\rho - 1}} + b_s, \\ \Gamma &= a_g exp\left(-b_g R_\rho\right) + c_g, \\ K_{dd}^{Radko} &= F_s k_T \Gamma \end{aligned} \tag{32}$$

,where $a_s = 135.7, b_s = -62.75, a_g = 2.709, b_g = 2.513, c_g = 0.5128$. On the other hand, diffusive convection-induced thermal diffusivity was developed by [17].

$$K_{dd}^{Fedo} = 0.909\nu exp\left(4.6exp\left[-0.54\left(\frac{1}{R_\rho} - 1\right)\right]\right), \tag{33}$$

where ν is the kinematic viscosity of the seawater,$1.08 \times 10^{-6}[m^2/s]$.

Even when double-diffusive convection is strong, disruption can occur if turbulence is sufficiently intense. Therefore, it is necessary to take into account such situations when we consider the generation of temperature variance due to double diffusion.

According to [22], turbulence no longer isotropic in the phase of $\epsilon < 200\nu N^2$. Based on this result, we assumed that the double-diffusive convection is still effective to induce vertical thermal and salinity flux under the condition of $Re_b < 200$ and $|Tu| > 45°$,where $Re_b = \frac{\epsilon}{\nu N^2}$ is buoyancy Reynolds number and Tu is Turner angle. Conversely, we assumed that the turbulence will disrupt the double diffusive convection and the vertical fluxes are supported by turbulence under the condition of $Re_b > 200$ or $|Tu| < 45°$.

Ultimately, we obtained the turbulent flux $\langle u_t\theta_t\rangle \sim K_\rho \left(\frac{d\theta_m}{dz}\right)$ in the area of $Re_b > 200$ or $|Tu| < 45°$, and double diffusive flux $\langle u_d\theta_d\rangle \sim K_{dd} \left(\frac{d\theta_m}{dz}\right)$ in the area of $Re_b < 200$ and $|Tu| > 45°$.

The results are also discussed in the Appendix part when the criteria by $|Tu|$ and Re_b are set to 75° and 20, respectively.

2.7 Mesoscale temperature gradient

The mesoscale temperature gradient is computed by subtracting the temperature observed from the World Ocean Atlas 2018 (WOA18) from the observed temperature measured by Navis float and EM-APEX float. Since the observed temperature from these floats cannot resolve microscale temperature gradients, this method allows for the estimation of mesoscale temperature gradients. Therefore, the mesoscale component includes submesoscale flows on the order of O(0.1-100 km) and smaller internal waves in this analysis .

3 Results and Discussion

3.1 Physical properties

The potential temperature and salinity section of the Izu Ridge is shown in the Figure 7. The color scale represents potential temperature and salinity at the Izu Ridge. The abscissa and ordinate represent longitude and depth, and the solid line black line indicates isopycnals. After interpolating at $0.01\sigma_\theta$ intervals, the pressure along isopycnal is averaged and displayed on the ordinate as mean isopycnal pressure, as shown in the figure 8, so that the gradient along ordinate is a diapycnal gradient. Hereafter, all figures are shown with the ordinate as mean isopycnal pressure or depth. Looking at the Figure8, relatively low-salinity filament can be seen from the surface to the 25 σ_θ contour line. Such a structure may be created by isopycnal stirring mainly drivn by meso- and submesoscale flows (Nagai,2021[23]). In the Kuroshio Extension front, similar structures are observed under 26 σ_θ in the eastern section and right above $26.5\sigma_\theta$ in the western

section (Figure9). Thus, meso- and submesoscale flows may induce isopycnal stirring, creating an environment favorable for double-diffusive convection.

There seems to be no significant difference in the spatial distribution of turbulent kinetic energy dissipation rate ϵ and microscale temperature variance dissipation rate χ in the Izu Ridge (Figure 10). This suggests that turbulence contributes preferentially to the generation of microscale temperature variance. In fact, diffusive nitrate flux computed with the eddy diffusivity based on the shear probe data show similar magnitude and spatial distribution to that from high-resolution thermistor, supporting the above notion. On the other hand, there is a large difference in the spatial distribution of ϵ and χ in the Kuroshio Extension front, with ϵ showing little spatial variation throughout the section, while χ is very high, close to $10^{-6}[^\circ C^2/s]$ over the mean isopycnal depths of 170m-400m(Figure 11). This suggests that temperature variance generation and dissipation within this depth range is occurring due to factors other than turbulence, such as double diffusive convection.

3.2 Diapycnal eddy diffusivity K_ρ, double-diffusion induced thermal diffusivityK_{dd}, and isopycnal stirring coefficient, K_e

The top panel of Figure 12 shows the diapycnal eddy diffusivity for areas where the buoyancy Reynolds number Re_b is greater than 200 or the absolute value of Turner angle Tu is less than 45°, and the middle panel shows the thermal diffusivity due to double diffusion for areas where the buoyancy Reynolds number Re_b is less than 200 and the absolute value of Turner angle Tu is greater than 45°. The bottom panel shows the isopycnal stirring coefficient calculated from the microscale temperature variance budget. The area with no values in the isopycnal stirring coefficient panel occurs when the microscale temperature variance generation rate due to turbulence and double diffusion acting against the mean temperature gradient $-K_\rho \left|\nabla_{||}\theta_m\right|^2 - K_{dd}\left|\nabla_{||}\theta_m\right|^2$ is larger than the microscale temperature dissipation rate $-\frac{\chi}{2}$. This may be caused by underestimation of χ or changes in mixing coefficient Γ, which is assumed here as 0.2, due to the existence of double diffusive convection which creates additional microscale vertical heat flux. Diapycnal diffusion due to turbulence is large just above the Izu Ridge, with diapycnal eddy diffusivity as large as $10^{-4} - 10^{-3}$ In contrast, diapycnal diffusion due to double diffusive convection is expected to be small, and the parameterized thermal diffusivity K_{dd} is less than $10^{-5.5}$ $\mathrm{m^2 s^{-1}}$ in most of the section. The isopycnal stirring coefficient K_e shows the values of $10^2 - 10^3$ $\mathrm{m^2 s^{-1}}$. Figure13 is same as Figure 12, but in the Kuroshio Extension front.

In the Kuroshio Extension front, vertical diffusion due to turbulence is small, but the vertical diffusion due to double diffusion is large throughout the section, nearly 10^{-4} $\mathrm{m^2 s^{-1}}$ of thermal diffusivity is found in the 300-400 m isopycnal mean depth band. High values of isopycnal stirring

by mesoscale eddies were estimated at depths greater than 200 m. In particular, values close to 10^4 m^2s^{-1} observed at 144-144.5°E around 380 m coincide with the regions where characteristics thermohaline interleaving structures were observed, suggesting that isopycnal stirring by mesoscale eddies creates an environment favorable for double-diffusive convection.

These values averaged over the longitude are shown in the Figure 14 for Izu Ridge (dashed line) and for Kuroshio Extension (solid line).

At the Izu Ridge, strong vertical mixing with vertical eddy diffusivities exceeding 10^{-5} m^2s^{-1} occur in the upper 170 m, which is 1 to 2 orders of magnitude greater than that of the Kuroshio Extension. As for the parameterized double diffusion induced thermal diffusivity, the Kuroshio Extension is nearly one order of magnitude larger than the Izu Ridge at the mean isopycnal depth 200-400 m. Similarly, isopycnal stirring coefficient is nearly 1-1.5 orders of magnitude greater in the Kuroshio Extension. Therefore, it is suggested that more active vertical mixing by double diffusive convection that is presumably supported by the strong isopycnal stirring by mesoscale eddies occurs in the Kuroshio Extension than the Izu Ridge especially at the mean isopycnal depth of 200-400 m. On the other hand, more active vertical mixing by turbulence especially in the upper 200 m occurs in the Izu Ridge compared to that in the Kuroshio Extension.

3.3 Microscale temperature variance generation rate via mesoscale temperature variance generation.

The microscale temperature variance generated by turbulence and double diffusion acting on the mean temperature gradient were compared with those generated via mesoscale variance. The upper panel of the Figure 15 and Figure 16 represents the microscale temperature variance generation rate by turbulent and double-diffusion acting on the mean temperature gradient, $K_\rho \left|\nabla_\perp \theta_m\right|^2, K_{dd} \left|\nabla_\perp \theta_m\right|^2$ in the Izu Ridge and the Kuroshio Extension front, respectively. The lower panel is the mesoscale temperature variance generation rate $K_e \left|\nabla_{||} \theta_m\right|^2$, which is transferred to microscale temperature variance generation by turbulence and double-diffusion acting on the mesoscale temperature gradient$\langle K_\rho \left|\nabla_\perp \theta_m\right|^2\rangle$,$\langle K_{dd} \left|\nabla_\perp \theta_m\right|^2\rangle$.

In the upper 200 m of the Izu Ridge, the direct temperature variance generation due to turbulence and double diffusion acting on the mean temperature gradient is dominant, with some values exceeding 10^{-6} [$°C^2s^{-1}$]. On the other hand, the mesoscale temperature variance generation rate due to mesoscale eddies acting on the mean temperature gradient is small throughout the section. Similar to the Izu Ridge, microscale temperature variance generation from the mean temperature gradient by turbulence and double diffusion is dominant in the upper 170 m of the Kuroshio Extension front. On the other hand, at the mean isopycnal depths deeper than 170 m, the mesoscale temperature variance generation by mesoscale eddies is dominant. It is suggested

that isopycnal stirring by mesoscale eddies are active in the Kuroshio Extension front, and that much microscale temperature variance are generated by double diffusion and turbulence against the mesoscale temperature variance provided by the along isopycnal stirring by mesoscale flows. In contrast to the Kuroshio Extension front, mesoscale eddies at the Izu Ridge are not active and turbulence acted directly on the mean temperature gradient to produce microscale temperature variance.

3.4 The comparison of temperature variance generation rate by turbulence and double diffusive convection acting on the mean and mesoscale temperature gradient.

Figure 17a compares the generation of microscale temperature variance resulting from turbulence acting on the mean temperature gradient and on the mesoscale temperature gradients at the Izu Ridge. Figure17b is the same as Figure 17a, but compares the microscale temperature variance generation rate due to double-diffusive convection.

At the Izu Ridge, both turbulence and double diffusion are found to generate microscale temperature variance by acting on the mean temperature gradient rather than acting on the mesoscale temperature gradient. However, in the upper layers where low-salinity water filaments are found, the microscale temperature variance generation rate due to double diffusion acting on the mesoscale temperature gradient was comparable in magnitude to that resulting from double diffusion acting on the mean temperature gradient. This suggests that double diffusive convection induced by low-salinity water stirred by mesoscale eddies generates microscale temperature variance by primarily acting on mesoscale temperature gradients.

The same parameters for the Kuroshio Extension are shown in Figure 18. In the upper 150 m of the Kuroshio Extension front, the microscale temperature variance generation rate primarily driven by turbulence acting on the mean temperature gradient reaches a relatively high value of $10^{-7}[^{\circ}C^2/s]$. However, it is still an order of magnitude less than that of the upper layer of the Izu Ridge. In contrast, the microscale temperature variance generation by double diffusion acting on the mesoscale temperature gradient is dominant under 150 m reaching about $10^{-7.5}[^{\circ}C^2/s]$. This is higher by 3 orders of magnitudes than that of the Izu Ridge. This result indicates that double diffusive convection can act on the mesoscale temperature gradient formed by isopycnal stirring, and generate abundant microscale temperature variance in the Kuroshio Extension front.

3.5 Comparison between mesoscale temperature variance generation rate and microscale temperature variance generation rate from mesoscale temperature

Mesoscale temperature variance generation rate $K_e \left|\nabla_{||}\theta_m\right|^2$ indirectly derived from the temperature variance budget equation was compared with the microscale temperature variance generation rate $\langle K_\rho \left|\nabla_\perp \theta_e\right|^2\rangle + \langle K_{dd} \left|\nabla_\perp \theta_e\right|^2\rangle$ directly calculated from mesoscale temperature gradient. The green and magenta lines in the Figure 19a represent the mesoscale temperature variance generation rate estimated from temperature variance budget equation and the microscale temperature variance generation rate by double-diffusion and turbulence acting on the mesosale temperature gradient in the Izu Ridge, respectively. The parameters in the Figure 19b are the same as those in Figure 19a, but in the Kuroshio Extension front.

While these 2 parameter values show the same orders of magnitude in the Kuroshio Extension, the mesoscale temperature variance generation rate is approximately 2 orders of magnitude greater in the Izu Ridge. There are two possible reasons for the discrepancy between these values at the Izu Ridge. One is that the additional generations of microscale temperature variance through the advection term may increase χ, thereby overestimating the mesoscale temperature variance generation term $K_e \left|\nabla_{||}\theta_m\right|^2$. The trajectory of Navis-MR float observation at the Izu Ridge (Figure1) suggests that the Kuroshio connects to the first meander of the Kuroshio Extension in the eastern part of the section which may reduce the horizontal transport of microscale temperature variance, while the microscale temperature variance generation is active in the western part of the section because of the turbulence generated by Kuroshio flowing over the seamount. Considering these factors, the advection term may tend to be positive and not be negligible. Another reason is the underestimation of microscale temperature variance generation rate through turbulence and double-diffusion acting on the mesoscale temperature gradient which might be caused by ignoring the horizontal generation term $\langle K_\rho \left|\nabla_{||}\theta_e\right|^2\rangle$. Although the triple decomposition frame work we employed ignores the generation of microscale thermal variance directrly from horizontal temperature gradient, it has been reported that the horizontal generation term may not be negligible in the front region (Gregg 1987 [3], Ruddick et al.2010[4]). Both the NavisMR and EM-APEX floats at the Kuroshio Extension front and the NavisMR float at the Izu Ridge are advected by the Kuroshio Extension and the Kuroshio where these jets are associated with the steep front (Figure2 and 1). Therefore, the these sections are expected to have large horizontal mesoscale temperature gradient in the direction across the front, which may have resulted in a non-negligible horizontal generation term. Unfortunately, our along-frontal observations did not allow for the calculation of temperature gradient across the front, preventing the calculation of microscale temperature vari-

ance generation due to turbulence acting against the isopycnal mesoscale temperature gradient $\langle K_\rho \left|\nabla_{||}\theta_e\right|^2\rangle$. Under the original assumption that the advection term can be neglected, this inconsistency implies that the horizontal generation term is approximately 2 orders of magnitude larger than the vertical generation term along the front in the Izu Ridge. However, this is unlikely as this indicates that the slope of isothermal $dz/dx = (\partial T/\partial x)/(\partial T/\partial z) \sim 100$ given that turbulence is isotropic. Thus, it is suspected that advective transport of microscale thermal variance that is generated by the Kuroshio flowing over Izu Ridge influences the thermal variance terms, leading to the inconsistency between mesoscale thermal variance generation term by isopycnal stirring and microscale thermal variance generation by microscale mixing processes. Additionally, isopycnal stirring coefficient K_e and mesoscale temperature variance generation rate $K_e \left|\nabla_{||}\theta_e\right|^2$ in the Izu Ridge may actually be smaller than the values we got in this study.

4 Conclusion

We have quantified the intensity of isopycnal stirring, considering the contribution of double-diffusive convection as well as turbulence to the diapycnal mixing, and shown that the pathways of tracer variance dissipation through various processes with different scales, such as microscale temperature variance generated by microscale processes from mean and mesoscale temperature fields, and mesoscale temperature variance generated by lateral stirring from mean temperature filed. The isopycnal stirring coefficient K_e ranges from 10^3 to $10^4[m^2/s]$ below 200 m depth in the Kuroshio Extension front and from 10^2 to $10^3[m^2/s]$ in the Izu Ridge. The values in the Kuroshio Extension front are approximately an order of magnitude larger than that in the Izu Ridge (Figure 14). This reflects much higher eddy activity in the Kuroshio Extension than that in the Izu Ridge. The thermohaline structure below 200 m depth in the Kuroshio Extension is characterized by both low-salinity, low-temperature water originated from Oyashio and high-salinity, high-temperature water attributed to the Kuroshio (Figure 3,9). These results implies that mesoscale fluctuation below 200 m depth induces thermohaline intrusion, leading to the formation of vertical gradient in mesoscale temperature in the Kuroshio Extension. Furthermore, the microscale temperature variance generation below 200 m depth was dominated by double diffusive convection acting on the mesoscale temperature gradient, with the generation rate approximately $10^{-7.5}[^\circ C^2/s]$ (Figure18b), indicating that double diffusive convection can act on the mesoscale temperature gradient formed by the isopycnal stirring and generate abundant microscale temperature variance. These results support the conclusions of Joyce (1977) [5] and Nagai et al.(2015)[6].

On the other hand, in the top 200 m depth of the Kuroshio Extension, the microscale turbulence acting on both mean and mesoscale temperature gradients are the dominant term that generates

microscale temperature variance. This microscale turbulence dominance in generating microscale temperature variance is also seen in the Izu Ridge.

With only one thousand km apart, the Kuroshio in the Izu Ridge and the Kuroshio Extension exhibit very different characteristics in generating and dissipating the temperature variance. The difference is attributed to the fact that the warm-saline Kuroshio waters encounter flesh-cold Oyashio related waters in the subsurface layer along the Kuroshio Extension in which meso- and submesoscale isopycnal stirring intensifies mingling of these two water masses laterally promoting the temperature variance generation and dissipation. This is of particular importance to understand the tracer variance generation, dissipation and associated vertical fluxes including nutrients. How these multiscale processes act on the across-gyre nutrient fluxes, enhancing the biological pump, and CO_2 flux? These should be answered by future studies.

5 Appendix

5.1 Assessment of the results when the threshold for double-diffusive convection dominance is tightened

In this study, we proceeded with the analysis under the assumption that temperature variance generation in areas where the absolute value of the Turner angle exceeds 45° and the buoyancy Reynolds number is less than 200 is attributed to double diffusion, while in other areas, it is due to turbulence. However, it is likely that double diffusion is hardly occurring in regions where Turner angle is close to 45 °. Therefore, we adjusted the Turner angle criteria to 75° and presented the results in Figure 20 for Izu Ridge and Figure 21 for Kuroshio Extension. In the Izu Ridge, the microscale temperature variances are hardly generated by double-diffusive convection except in the upper layer where a low salinity filament can be observed. Similarly, double-diffusive convection didn't generate any variance in the upper 150m in the Kuroshio Extension region. However, the conclusion remains unchanged that abundant microscale temperature variance is generated by double-diffusive convection acting on mesoscale temperature gradients below 150 meters in the Kuroshio Extension region.

5.2 Assessment of the results when the threshold for turbulent dominance is relaxed

Not only the assessment of double-diffusive convection dominance using the Turner angle Tu, but also the evaluation of turbulent dominance based on the buoyancy Reynolds number Re_b should be discussed. The temperature variance generation rates under the assumption that the turbulence

dominates double-diffusive convection in the area where $|Tu| < 45°$ or $Re_b > 20$ are shown in the Figure 22 for the Izu Ridge and Figure23 for the Kuroshio-Extension. Although temperature variance generation rates in the Izu Ridge show only minimal change, those due to turbulence increased, while those due to double-diffusive convection decreased in the Kuroshio Extension. Considering this change is ultimately due to a change in whether the microscale temperature variance generation in area where $20 < Re_b < 200$ and $|Tu| > 45°$ is caused by turbulence or double diffusion, we need to advance our understanding for the coexistence of turbulence and double-diffusive convection in order to more accurately distinguish their dominance.

6 Acknowledgement

I'm grateful to Prof. Takeyoshi Nagai for his instruction, as well as to my colleagues and professors in the Marine Resources and Environment course for their insightful discussions. I also wish to thank ocean physics group in University of Victoria (Canada) for providing the knowledge necessary to advance this study. The research was conducted with the support of scholarships by Academic Research in Marine Resources and Environment (Tokyo University of Marine Science and Technology) and Japan Student Services Organization.

References

[1] T. R. Osborn. Estimates of the local rate of vertical diffusion from dissipation measurements. *Journal of Physical Oceanography*, 1980.

[2] T.R. Osborn and C.S. Cox. Oceanic fine structure. *Geophysical Astrophysical Fluid Dynamics, 3, 321-345.*, 1972.

[3] Gregg M.C. Diapycnal mixing in the thermocline. *A review. J. Geophys. Res., 92(C5), 5249–5286.*, 1987.

[4] Oakey N. S. andHebert D. Ruddick, B. R. Measuring lateral heat flux across a thermohaline front: A model and observational test. *Journal of Marine Research, vol.68, no. 3-4, pp. 523-539*, 2010.

[5] Joyce T.M. A note on the lateral mixing of water masses. *J. Phys. Oceanogr., 7, 626–629.*, 1977.

[6] A.Tandon H.Yamazaki T.Nagai, R. Inoue. Evidence of enhanced double-diffusive convection below the main stream of the kuroshio extension. *J Geophys Res 120:8402–8421.*, 2015.

[7] Chris Garrett. Stirring and mixing: What are the rate controlling processes. In *Proc.'Aha Huliko'a Winter Workshop*, volume 1. University of Hawaii at Manoa, 2001.

[8] K. L. Polzin A. C. Naveira Garabato, R. Ferrari. Eddy stirring in the southern ocean. *J. Geophys.Res., 116,C09019*, 1972.

[9] Raffaele Ferrari Jan D. Zika Alberto C. Naveira Garabato, Kurt L. Polzin and Alexander Forryan. A microscale view of mixing and overturning across the antarctic circumpolar current. *J. Phys. Oceanogr., 46,233–254*, 2016.

[10] Dorleta Orúe-Echevarría1 and Alberto C. Naveira Garabato Alexander Forryan and Josep L. Pelegrí Josep L. Pelegrí, Kurt L. Polzin. Mixing and overturning across the brazil-malvinas confluence. *Journal of Geophysical Research: Oceans, 128, e2022JC018730.*, 2023.

[11] Kraichnan R. Small-scale structure of a scalar field convected by turbulence. *Phys Fluids 11:945–953*, 1968.

[12] Thompson K Ruddick BR, Anis K. Maximum likelihood spectral fitting: The batchelor spectrum. *J Atmos Oceanic Technol 17;1541-1555*, 2000.

[13] N.S Oakey. Determination of the rate of dissipation of turbulent energy from simultaneous temperature and velocity shear microstructure measurements. *J.phys.Oceanogr,12:256–271*, 1982.

[14] R.E. Davis. Diapycnal mixing in the ocean:the osborn-cox model. *J. Phys. Oceanogr., 24,2560-2576*, 1994.

[15] R.Ferrari and K.L.Polzin. Finescale structure of the t–s relation in the eastern north atlantic. *J. Phys. Oceanogr,35:1437–1454*, 2005.

[16] Smith DP Radko T. Equilliblium transport in double-diffusive convection. *J Fluid Mech 692;5-27*, 2012.

[17] Fedrov KN. Layer tickles and effective diffusivities in diffusive thermohaline convection in the ocean. *In;Nihoul J,Jmrt B (eds) Small-scale turbulence and mixing in the ocean.Elseviser, Amsterdam*, 1988.

[18] Thompson K Ruddick BR, Anis A. Maximum likelihood spectral fitting: The batchelor spectrum. *J . Atmos Oceanic Technol 17:1541-1555*, 2000.

[19] St. Laurent and R.W.Schmitt. The contribution of salt fingers to vertical mixig in the north atrantic tracer release experiment. *J. Phys. Oceanogr.,20,1404-1424*, 1999.

[20] Ruddick BR. A practical indicater of the stability of the water column to double-diffusive activity. *Deep sea Res 30:1105-1107*, 1983.

[21] Radko T. Double-diffusive convection. *Cambtidge University Press,Cambridge*, 2013.

[22] P.W.Nasmith A.E.Gargett, T.R.Osborn. Local isotropy and the decay of turbulence in a stratified fluid. *J . Fluid Mech.vol. 144, pp. 231-280*, 1984.

[23] T.Nagai. Elevated turbulent and double-diffusive nutrient flux in the kuroshio over the izu ridge and in the kuroshio extension. *J. Oceanogr,77:55–74*, 2021.

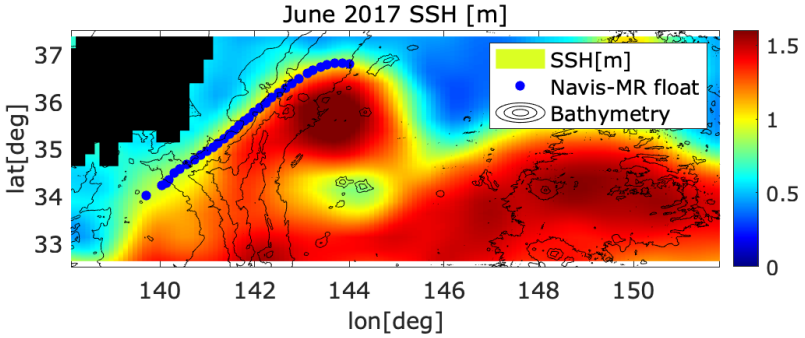

Figure 1: The trajectory of the (Blue)Navis-MR float on June 2017, over the Izu Ridge. The shaded area denotes the sea surface height [m] averaged over June 2017. The contour represents bathymetry from 0 to 8000 meters, in increments of 2000 meters.

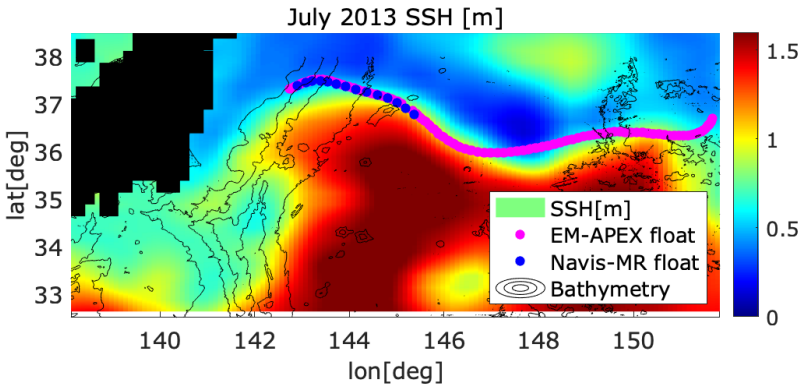

Figure 2: The trajectory of the (Blue) Navis-MR float and (Magenta)EM-APEX float on July 2013, along the Kuroshio Extension.The shaded area denotes the sea surface height[m] averaged over July 2013.The contour represents bathymetry from 0 to 8000 meters, in increments of 2000 meters.

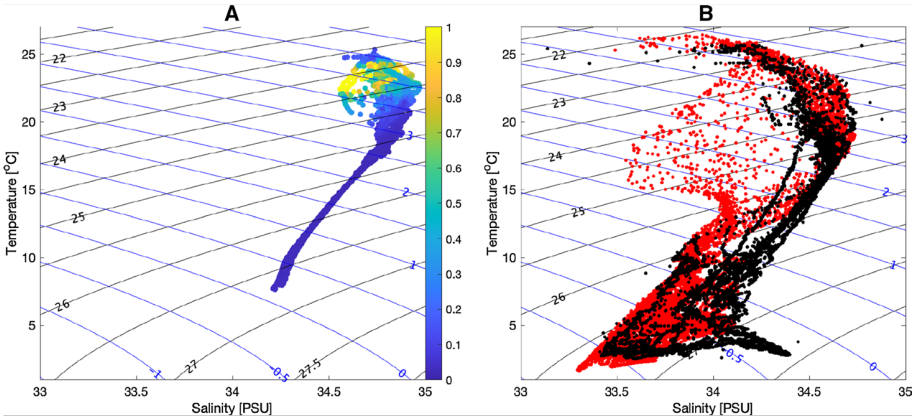

Figure 3: Nagai et al. (2021)[23],Figure5: Temperature–Salinity diagram for (a) June 2017 and (b) July 2013 cruises. Red and black points indicate data obtained by the EMAPEX float and the Underway-CTD, respectively in (b). The color shading in (a) indicates chlorophyll-a concentration [$\mu g L^{-1}$]. Black and blue contours are for isopycnals and isolines of the spiciness (Flament 2002), respectively.

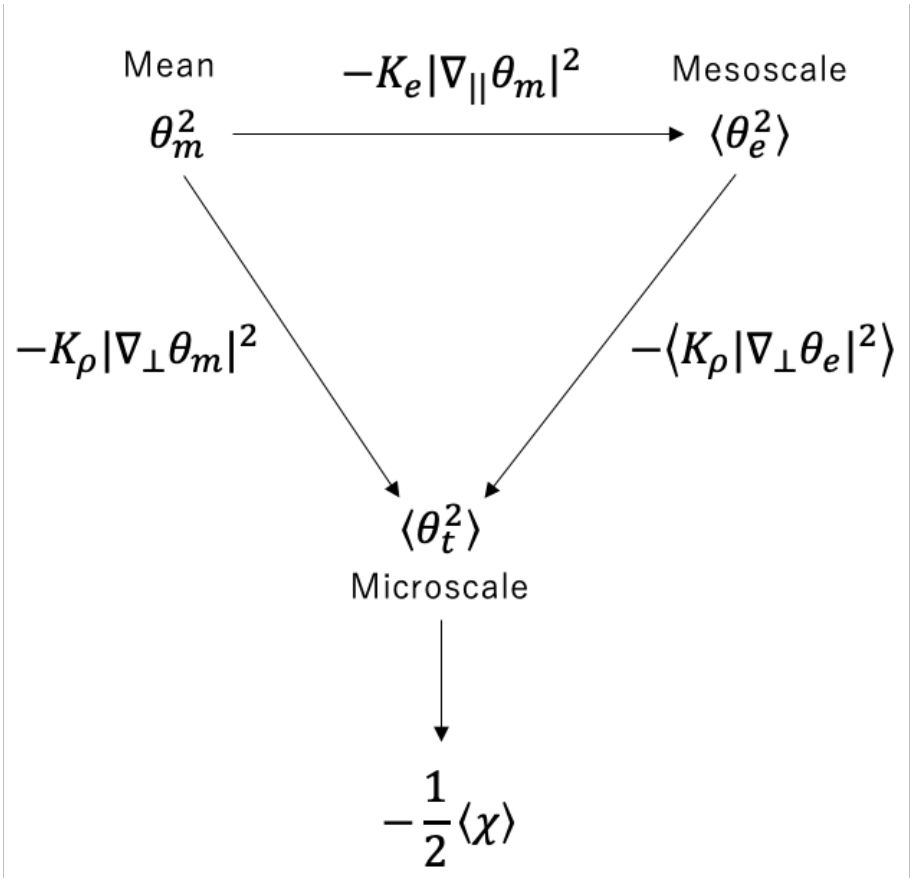

Figure 4: The schematics of the potential temperature variance transfer.

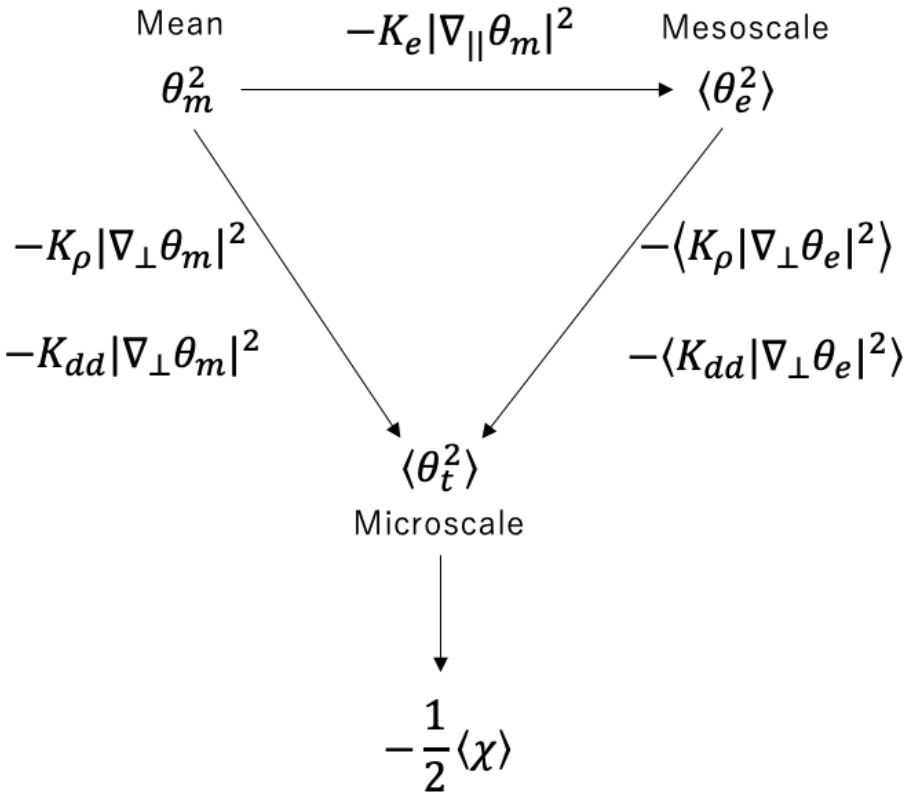

Figure 5: The schematics of the potential temperature variance transfer considering double diffusive convection.

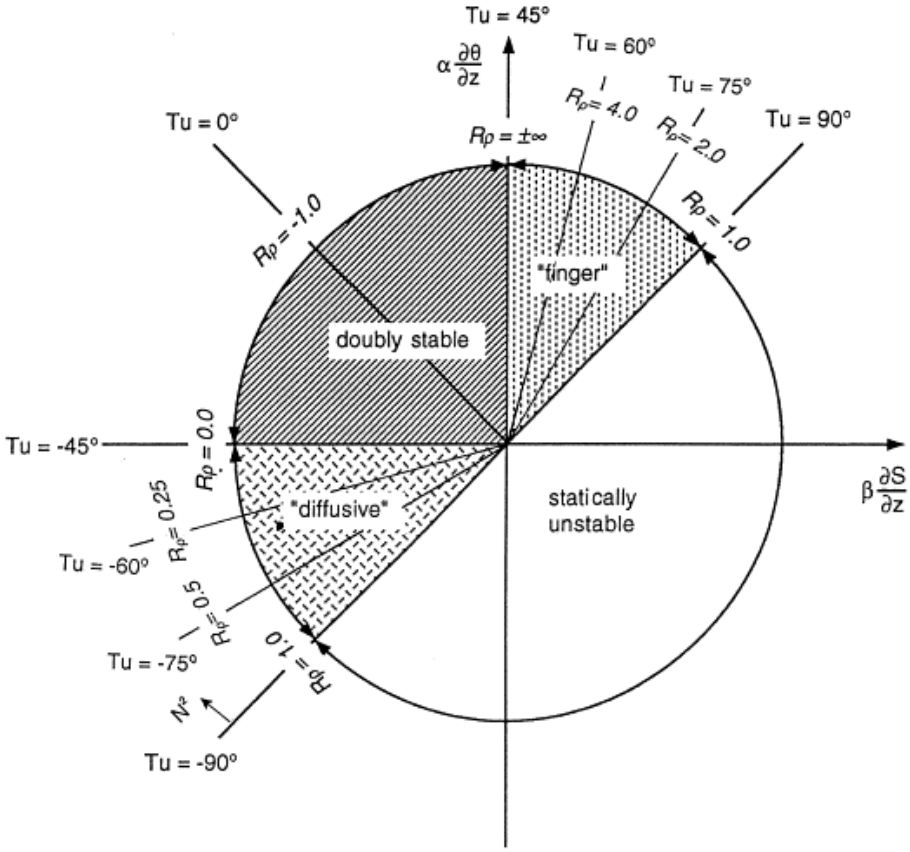

Figure 6: Yuzhu You (2002),Figure3: Definition of the Turner angle, Tu (degree), with corresponding R_ρ value.

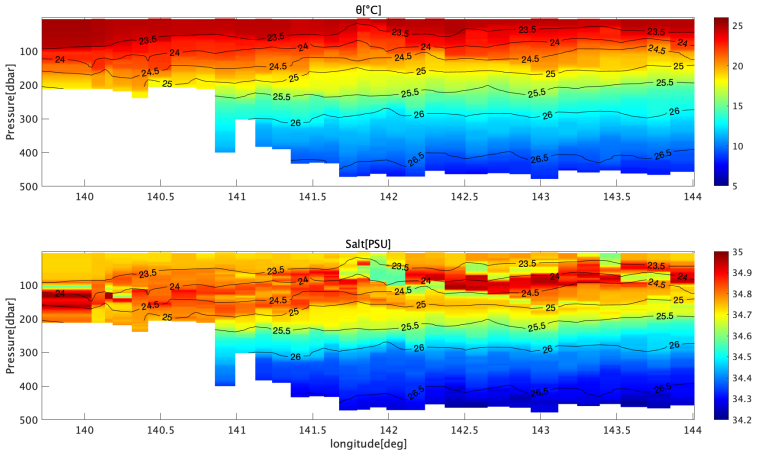

Figure 7: Potential temperature[$°C$] and salinity[PSU] section in the Izu Ridge.

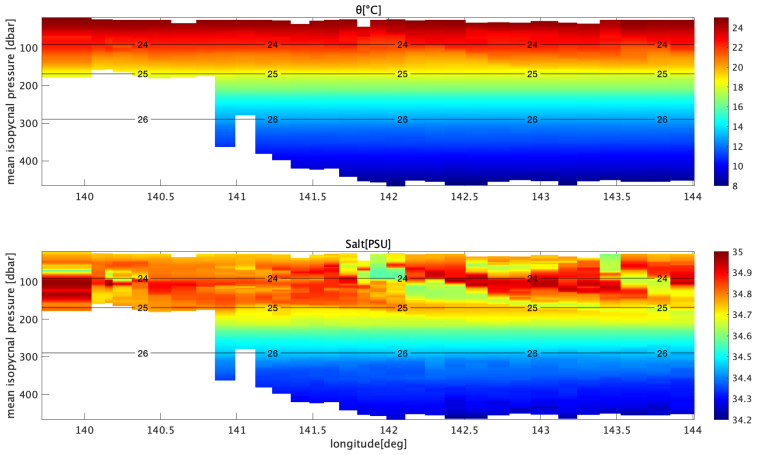

Figure 8: Potential temperature[$°C$] and salinity[PSU] section in the Izu Ridge. Note that the vertical axis represents the depth averaged along the isopycnal line.

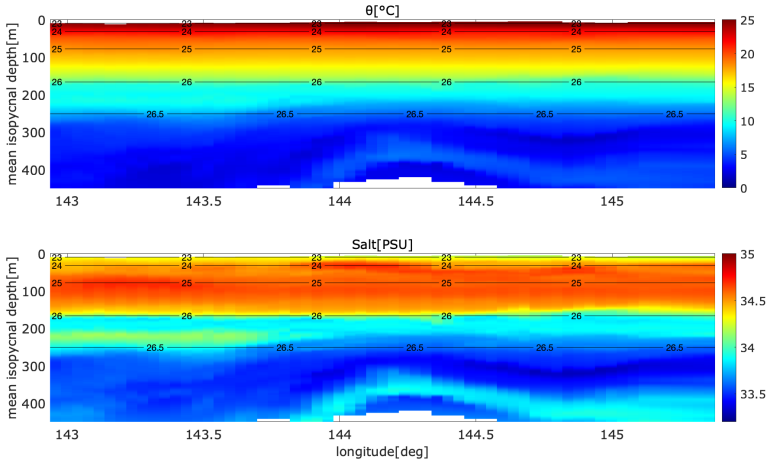

Figure 9: Potential temperature[$°C$] and salinity[PSU] section along the Kuroshio Extension front.

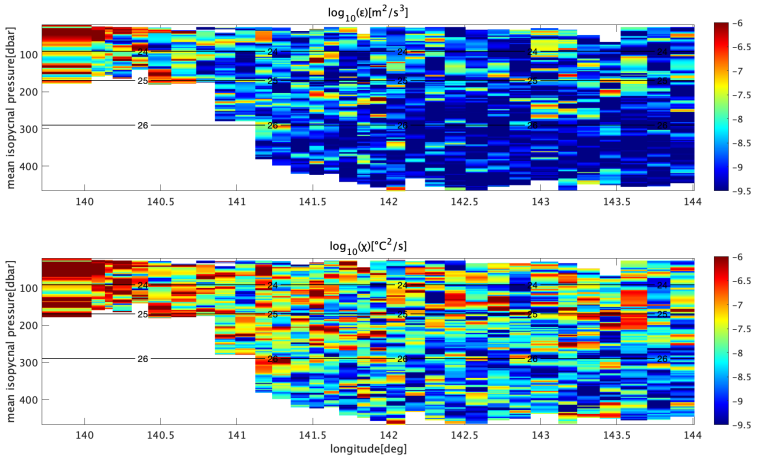

Figure 10: TKE dissipation rate $log_{10}(\epsilon)$ $[m^2/s^3]$ and Microscale temperature variance dissipation rate $log_{10}(\chi)[°C^2/s]$ section in the Izu Ridge.

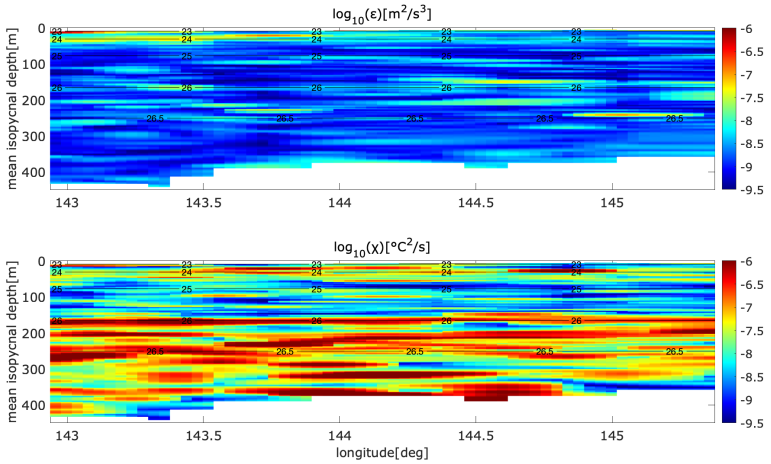

Figure 11: TKE dissipation rate $log_{10}(\epsilon)$ $[m^2/s^3]$ and Microscale temperature variance dissipation rate $log_{10}(\chi)[^\circ C^2/s]$ section along the Kuroshio Extension front.

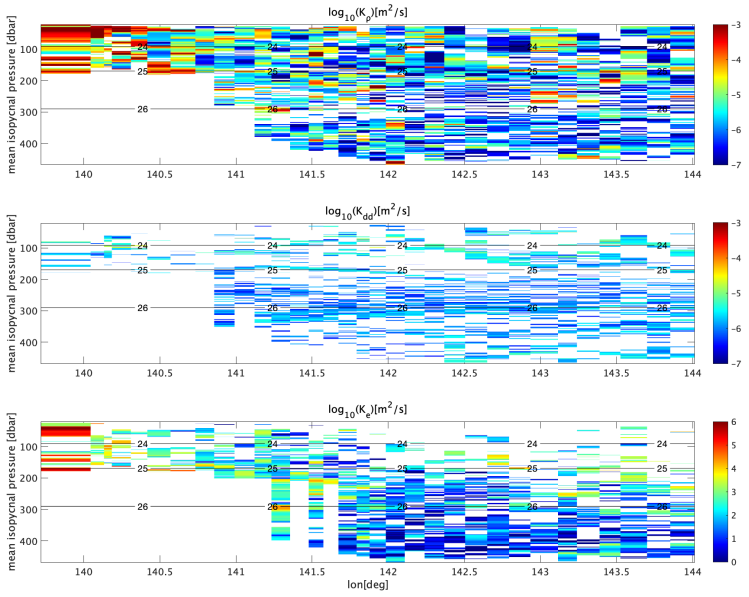

Figure 12: Diapycnal eddy diffusivity $log_{10}(K_\rho)$ $[m^2/s]$, double-diffusion induced temperature variance $log_{10}(K_{dd})$ $[m^2/s]$,and isopycnal stirring coefficient $log_{10}(K_e)$ $[m^2/s]$ section in the Izu Ridge.

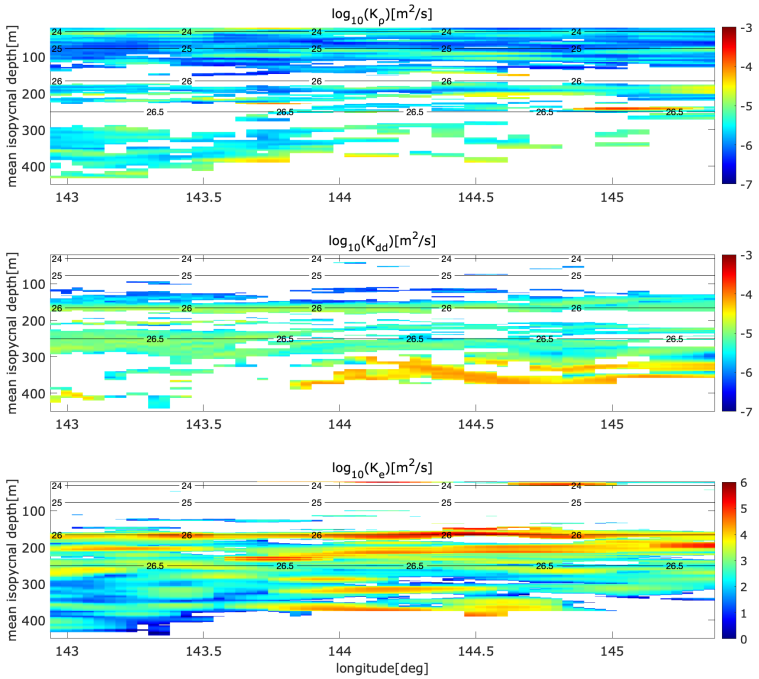

Figure 13: Diapycnal eddy diffusivity $log_{10}(K_\rho)$ $[m^2/s]$, double-diffusion induced temperature variance $log_{10}(K_{dd})$ $[m^2/s]$,and isopycnal stirring coefficient $log_{10}(K_e)$ $[m^2/s]$ section in the Kuroshio Extension.

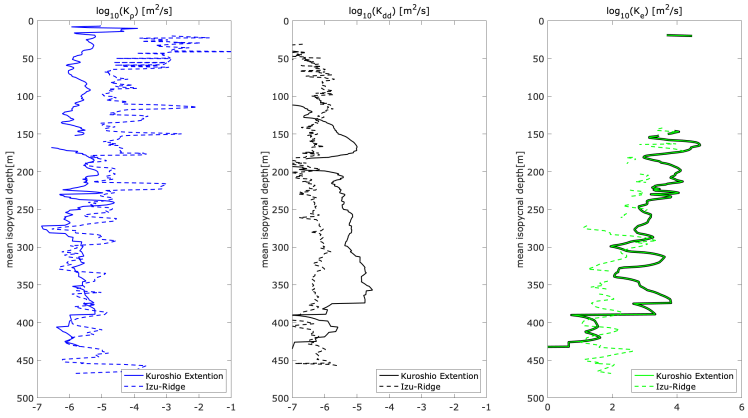

Figure 14: Diapycnal eddy diffusivity $log_{10}(K_\rho)$ $[m^2/s]$, double-diffusion induced temperature variance $log_{10}(K_{dd})$ $[m^2/s]$,and isopycnal stirring coefficient $log_{10}(K_e)$ $[m^2/s]$ profile averaged over the section in the Izu Ridge and Kuroshio Extension front.

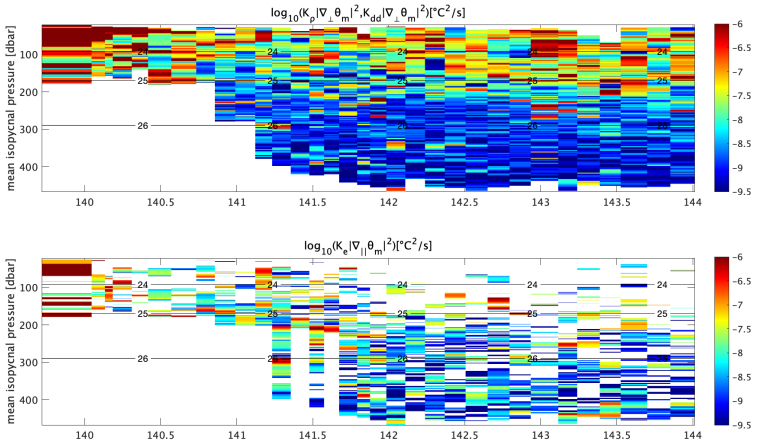

Figure 15: Microscale temperature variance generation rate directly from mean temperature gradient $log_{10}\left(K_\rho \left|\nabla_\perp \theta_m\right|^2, K_{dd} \left|\nabla_\perp \theta_m\right|^2\right)$ $[^\circ C^2/s]$ (upper panel) and mesoscale temperature variance generation rate $log_{10}\left(K_e \left|\nabla_{||} \theta_m\right|^2\right)$ $[^\circ C^2/s]$ (lower panel) section in the Izu Ridge.

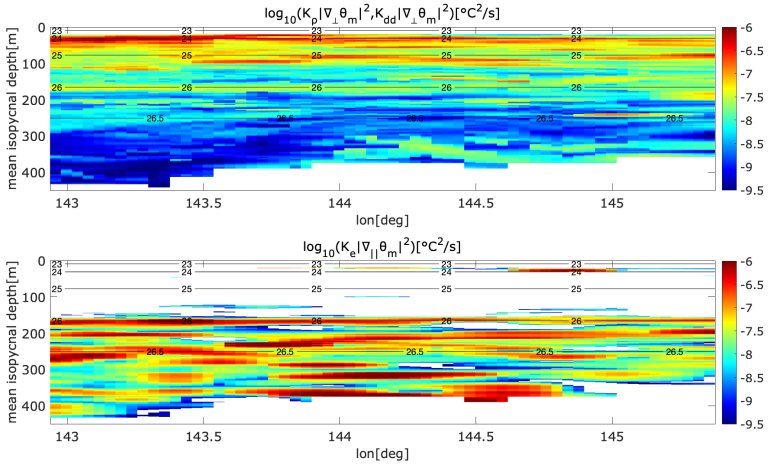

Figure 16: Microscale temperature variance generation rate directly from mean temperature gradient $log_{10}\left(K_\rho \left|\nabla_\perp \theta_m\right|^2, K_{dd} \left|\nabla_\perp \theta_m\right|^2\right)$ $[^\circ C^2/s]$ (upper panel) and mesoscale temperature variance generation rate $log_{10}\left(K_e \left|\nabla_{||} \theta_m\right|^2\right)$ $[^\circ C^2/s]$ (lower panel) section along Kuroshio Extension front.

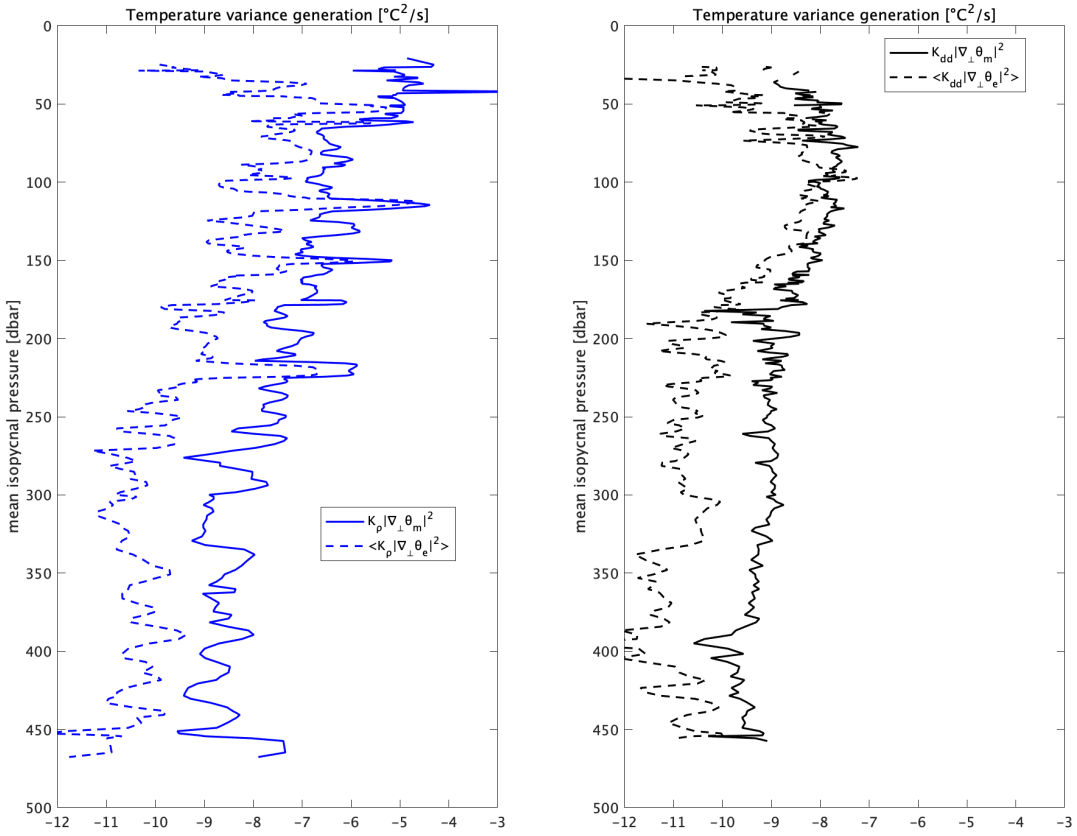

(a) (b)

Figure 17: Microscale temperature variance generation rate by (a)turbulence and (b)double diffusive convection acting on mean temperature gradient(solid line) and mesoscale temperature gradient(dashed line)at the Izu Ridge

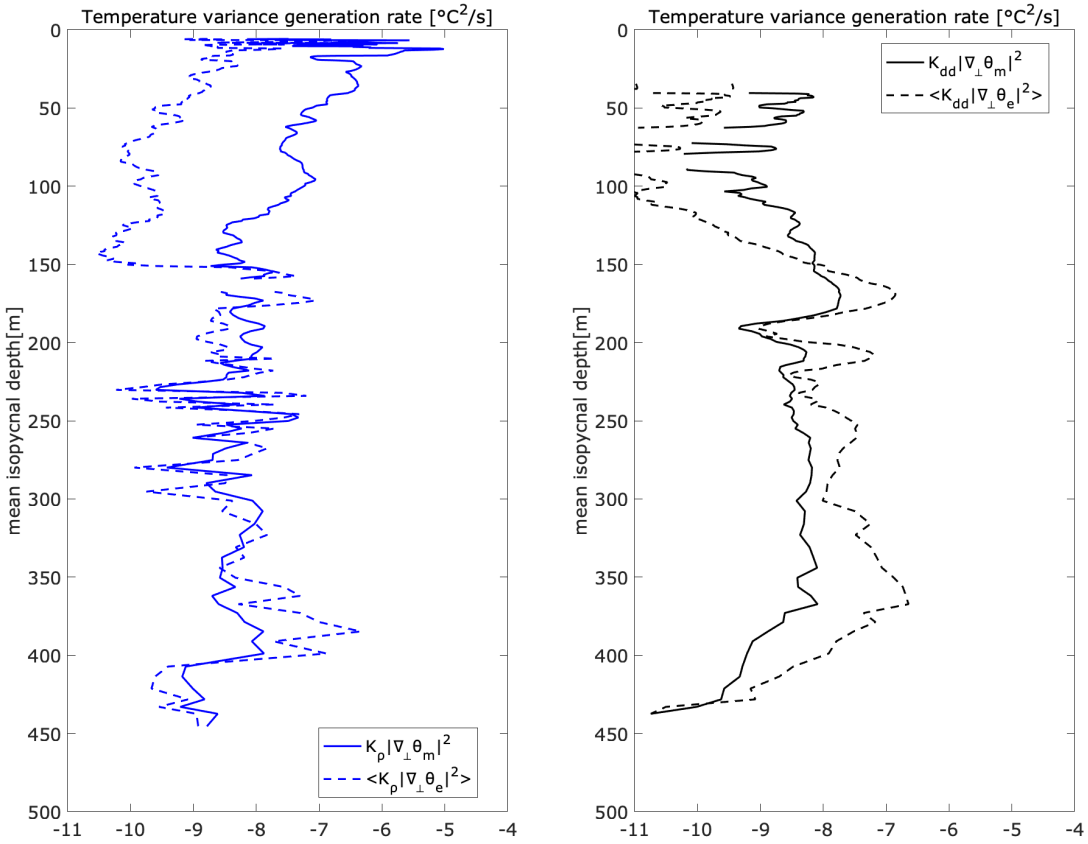

(a) (b)

Figure 18: Microscale temperature variance generation rate by (a)turbulence and (b)double diffusive convection acting on mean temperature gradient(solid line) and mesoscale temperature gradient(dashed line) at the Kuroshio Extension

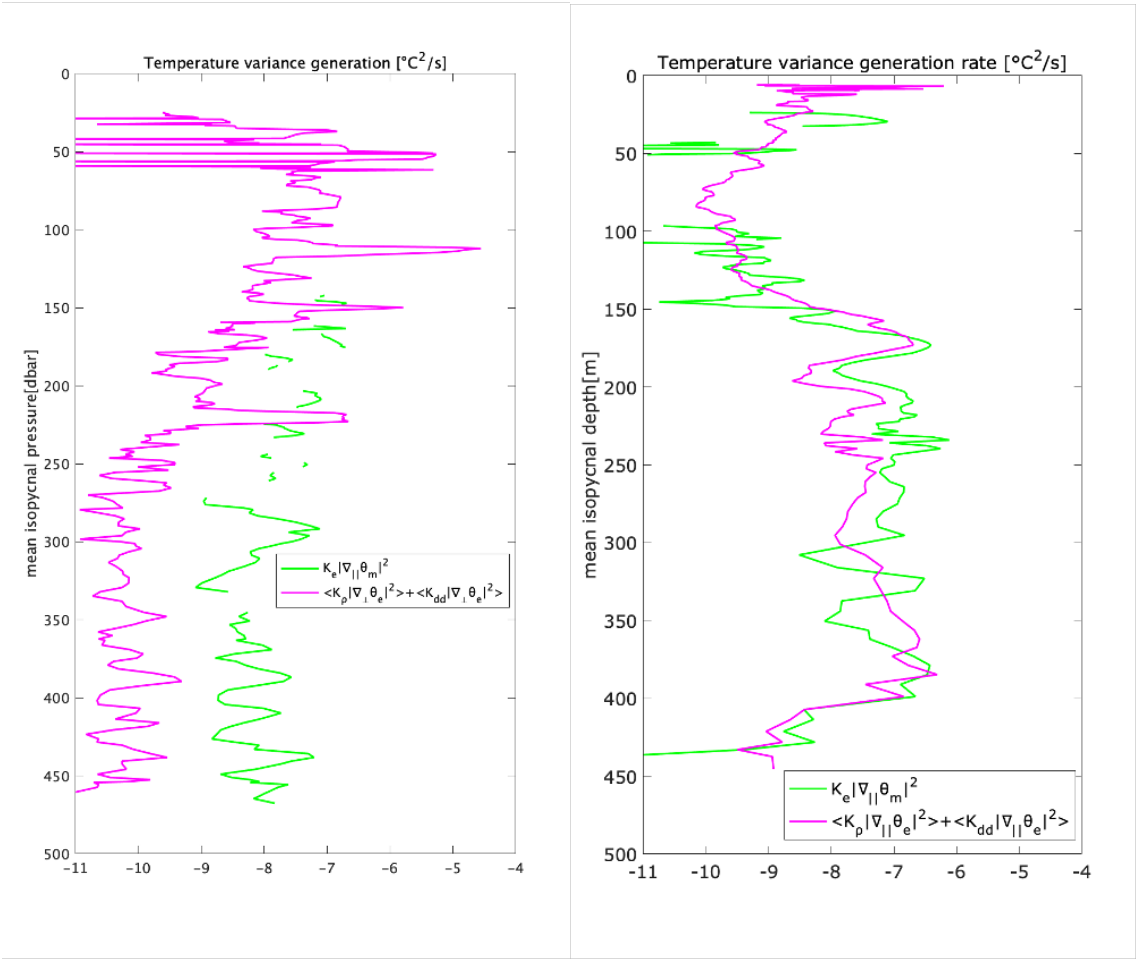

(a) (b)

Figure 19: Comparizon between mesocale temperature variance generation rate $K_e \left|\nabla_{||}\theta_m\right|^2$ (green) and microscale temperature variance generation rate from mesoscale temperature $\langle K_\rho \left|\nabla_\perp \theta_e\right|^2\rangle + \langle K_{dd} \left|\nabla_\perp \theta_e\right|^2\rangle$ (magenta) in the (a)Izu Ridge, and (b)Kuroshio Extension front.

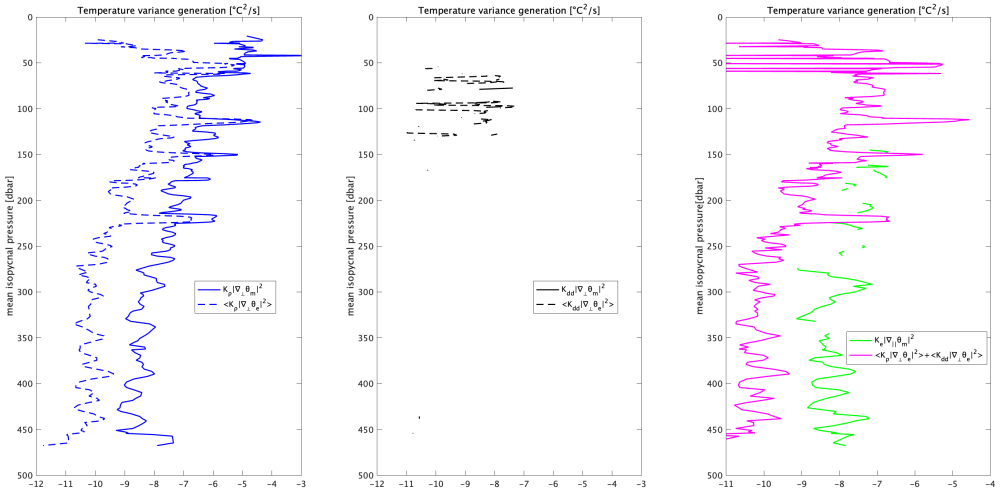

(a) (b) (c)

Figure 20: Microscale temperature variance generation rate by (a)turbulence and (b)double diffusive convection acting on mean temperature gradient(solid line) and mesoscale temperature gradient(dashed line) in the Izu Ridge. (c) Comparizon between mesoscale temperature variance generation rate $K_e \left|\nabla_{||}\theta_m\right|^2$ (green) and microscale temperature variance generation rate from mesoscale temperature $\langle K_\rho \left|\nabla_\perp \theta_e\right|^2\rangle + \langle K_{dd} \left|\nabla_\perp \theta_e\right|^2\rangle$ (magenta) in the Izu Ridge. All of these calculations are based on the assumption that the double-diffusive flux dominates microscale temperature variance generation in regions where $|Tu| > 75°$ and $Re_b < 200$.

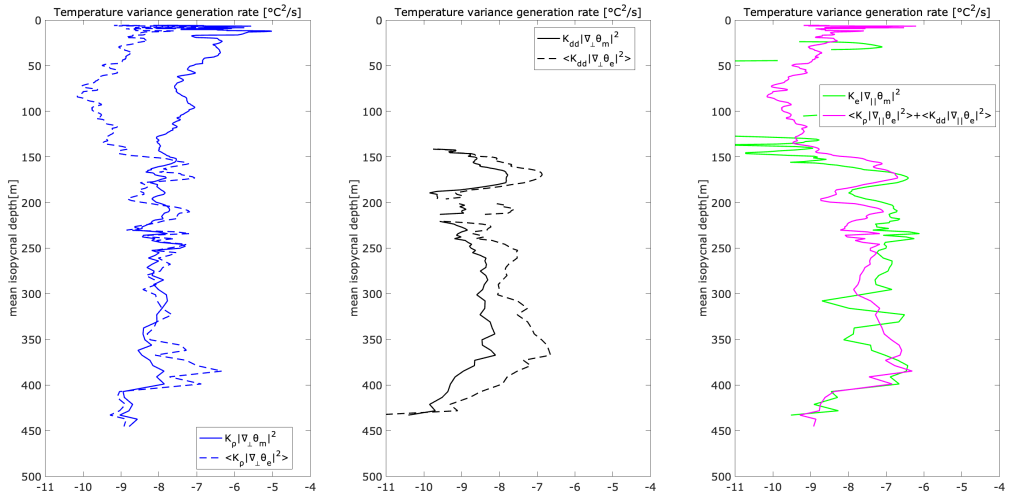

(a) (b) (c)

Figure 21: Microscale temperature variance generation rate by (a)turbulence and (b)double diffusive convection acting on mean temperature gradient(solid line) and mesoscale temperature gradient(dashed line) in the Kuroshio Extension. (c) Comparizon between mesoscale temperature variance generation rate $K_e \left|\nabla_{||}\theta_m\right|^2$ (green) and microscale temperature variance generation rate from mesoscale temperature $\langle K_\rho \left|\nabla_\perp \theta_e\right|^2\rangle + \langle K_{dd} \left|\nabla_\perp \theta_e\right|^2\rangle$ (magenta) in the Kuroshio Extension. All of these calculations are based on the assumption that the double-diffusive flux dominates microscale temperature variance generation in regions where $|Tu| > 75°$ and $Re_b < 200$.

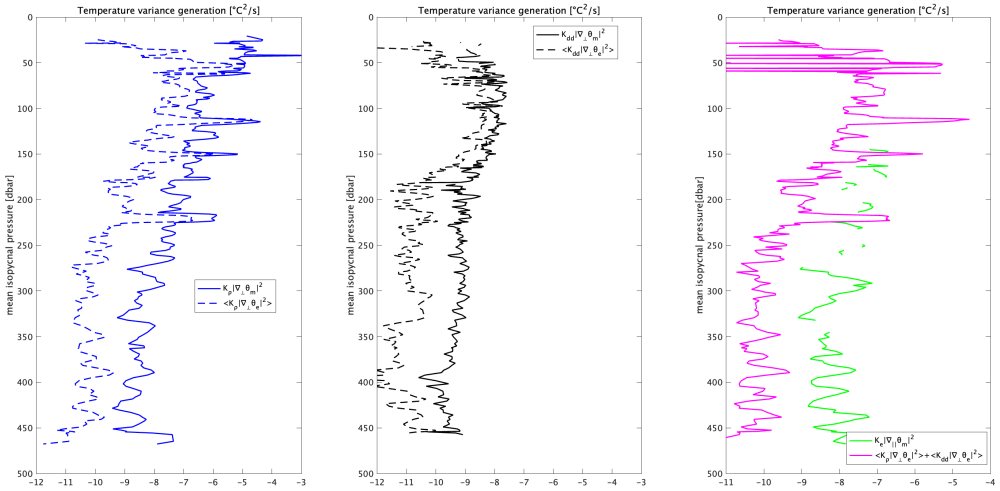

(a) (b) (c)

Figure 22: Microscale temperature variance generation rate by (a)turbulence and (b)double diffusive convection acting on mean temperature gradient(solid line) and mesoscale temperature gradient(dashed line) in the Izu Ridge. (c) Comparizon between mesoscale temperature variance generation rate $K_e \left|\nabla_{||}\theta_m\right|^2$ (green) and microscale temperature variance generation rate from mesoscale temperature $\langle K_\rho \left|\nabla_\perp \theta_e\right|^2\rangle + \langle K_{dd} \left|\nabla_\perp \theta_e\right|^2\rangle$ (magenta) in the Izu Ridge. All of these calculations are based on the assumption that the double-diffusive flux dominates microscale temperature variance generation in regions where $|Tu| > 45°$ and $Re_b < 20$.

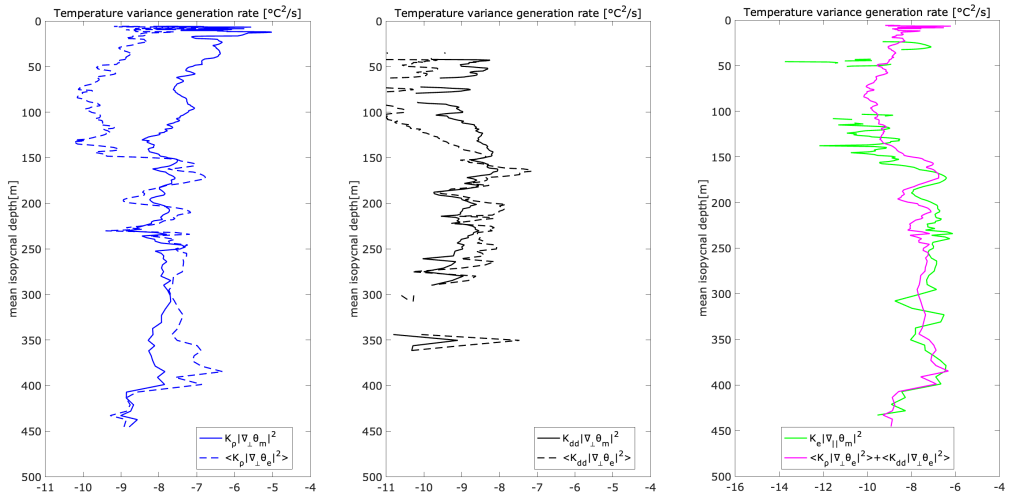

(a) (b) (c)

Figure 23: Microscale temperature variance generation rate by (a)turbulence and (b)double diffusive convection acting on mean temperature gradient(solid line) and mesoscale temperature gradient(dashed line) in the Kuroshio Extension. (c) Comparizon between mesoscale temperature variance generation rate $K_e \left|\nabla_{||}\theta_m\right|^2$(green) and microscale temperature variance generation rate from mesoscale temperature $\langle K_\rho \left|\nabla_\perp \theta_e\right|^2\rangle + \langle K_{dd} \left|\nabla_\perp \theta_e\right|^2\rangle$ (magenta) in the Kuroshio Extension. All of these calculations are based on the assumption that the double-diffusive flux dominates microscale temperature variance generation in regions where $|Tu| > 45°$ and $Re_b < 20$.